Article

Unveiling High-Tech Metals in Roasted Pyrite Wastes from the Iberian Pyrite Belt, SW Spain

Lola Yesares [1,*], José María González-Jiménez [2], Francisco Abel Jiménez-Cantizano [3,4], Igor González-Pérez [5], David Caro-Moreno [3] and Isabel María Sánchez [6]

[1] Departamento de Mineralogía y Petrología, Facultad de Ciencias Geológicas, Universidad Complutense de Madrid, C/José Antonio Nováis 12, 28040 Madrid, Spain

[2] Instituto Andaluz de Ciencias de la Tierra (CSIC-UGR), Avda. Palmeras 4, 18100 Armilla, Spain; jmgonzj@ugr.es

[3] Agencia de Medio Ambiente y Agua, Junta de Andalucía, C/Johan G. Gutenberg, 41092 Sevilla, Spain

[4] Departamento de Ciencias Analíticas, Facultad de Ciencias, Universidad Nacional de Educación a Distancia (UNED), Senda del Rey 9, 20840 Madrid, Spain

[5] Departamento de Mineralogía y Petrología, Facultad de Ciencias, Universidad de Granada, Avda. Fuentenueva s/n, 18001 Granada, Spain

[6] Centro de Instrumentación Científica, Universidad de Granada, Paseo Profesor Juan Osorio, s/n, 18071 Granada, Spain

* Correspondence: myesares@ucm.es

Abstract: The Iberian Pyrite Belt (IPB), in the southwestern Iberian Peninsula, is a large metallogenic province exploited since ancient times. As a result of historical and current mining activity, a vast volume of metallic mineral waste, mainly derived from the processing of pyrite, is still in situ and polluting the environment. A specific mine waste residuum locally known in the area as "morrongos", which was produced during pyrite roasting mainly in the 19th century, is evaluated here in order to unravel untapped resources of high-tech metals commonly used in high-tech devices. Applying a combination of whole-rock geochemical (ICP-AES, ICPMS, FA-AAS) and single-grain mineralogical techniques (EPMA, LA-ICP-MS, FESEM, and FIB-HRTEM) on the "morrongos", we unhide the still-present remarkable concentrations of Au, Ag, Pb, Zn, and Cu in them. The mineralogical expressions for these economic metals include oxides (hematite, magnetite, and hercynite), arsenates, sulfates of the jarosite group, native metals, and, to a lesser extent, relictic sulfides. This first-ever estimation of these economic metals in this type of residue allows their revalorization, highlighting them as suitable sources for the exploitation and recovery of metals necessary for the clean energy transition.

Keywords: mine waste; roasted pyrite; Iberian Pyrite Belt; high-tech metals; untapped resources; circular economy; mineralogical waste characterization

1. Introduction

These days, our daily lives in a connected and environmentally sustainable world boost the development of new high-tech and green-tech technologies, which are progressively requiring new metals in significant economic and strategic sectors. For example, manufacturing batteries, construction tools, sensors, electronic devices, medical devices, metals, automotive, defense, or renewable energy sectors. With a rising global population, the demand for metals necessary for these technological applications will grow ever greater [1,2]. However, the natural resources of many of the metals necessary for this technological progress are limited to a very few countries, which means that in the near future, many developed countries will not be able to reach the self-supply of certain metals. Thus, some metals are acquiring the category of "critical" or "strategic" for many developed countries [3], commonly including the platinum-group elements (PGE: Os, Ir, Ru, Rh, Pt, Pd), rare earths of the heavy (HREE: Eu, Gd, Tb, Dy, Ho, Er, Tm, Yb, Lu) and light (LREE: La, Ce, Pr, Nd, Pm, Sm) subgroups, as well as Cu, Ni, Co, Li, Sb, Bi, Nb, Ta, W, Ge, Ti, and

Ga. Other metals, identified as non-critical but that are also essential to the functioning and integrity of a wide range of industrial ecosystems, include the ferrous (Cr, Fe, W) and non-ferrous (Al, Pb, Sn, Sr, Zn, Mo, Ag, Au) metals, which collectively with the critical ones are named as high-tech metals [4].

As noted, high-tech metals are concentrated in specific regions of the Earth's crust. For instance, 90% of PGE production is in the Republic of South Africa [5], where the PGE are concentrated in magmatic deposits of Ni-Cu sulfides and Cr oxides, resulting from the injection of mantle-derived ultrabasic magmas into the continental crust. Almost 70% of globally available Co resources are within the Democratic Republic of the Congo [6] in hydrothermal-related sedimentary-hosted deposits. The global market for REE targets the extraction and manufacturing of ores related to alkaline-carbonatite igneous rocks [7] and granitic pegmatites [8]. In addition, the extraction, concentration, and metallurgy of minerals usually endowed with several high-tech metals in primary deposits are becoming more difficult and expensive.

Facing this concern over high-tech metal supply reliability and its further implications, diversifying supplies of high-tech metals is perhaps the only solution for many countries. For instance, in Europe, the Circular Economy Action Plan [9] is an ambitious but concrete program that stimulates Europe's transition towards a Circular Economy by contributing to 'closing the loop' of product life cycles. The measures in the action plan cover the whole life cycle of products, from production and consumption to waste management, as well as the market for secondary raw materials (SRM). Innovation and investment in the field have been promoted through the H2020 program in Europe. Moreover, similar environmental, social, and governance actions are being implemented in many other developed countries in order to further strengthen both reuse and recycling as well as the recovery of SRMs, e.g., [10–12]. A secondary market for high-tech metals is now promised by incoming policies. Hence, SRMs would provide a strategic resource of high-tech metals for many countries. Aiming to achieve a scenario of maximum reuse and recycling of high-tech critical metals, many state-funded agencies, often in collaboration with private companies, are seeking alternatives in the greenfield of urban and mining wastes, e.g., [13]. Urban waste has been suggested as a worthy target to overcome the near future demand for metals [14]. However, global recycling rates of many of the high-tech metals in urban waste are low (<5% for Ge, Li, or REE as an example [15,16]), while their reuse is often hindered by fabrication barriers (i.e., miniaturization). Therefore, these alternatives are still substantially insufficient to meet the incoming demand for high-tech metals.

In the scenario exposed above, mine wastes are seen as a more attractive source for metal recovery [17–20]. In particular, pyritic-rich mining-waste rocks, representing a global risk for environmental pollution due to their enormous potential to produce acid drainage mine (ADM), seem to still contain profitable amounts of many tech metals [21–23]. On this line, the application of mineralogical characterization to these types of mine wastes has the potential to reduce the environmental risk due to the recovery of the minerals, guide appropriate mine planning for active mines, optimize remediation design at closed or abandoned mines, and revalorize untapped resources of metals of current economic value [24].

The Iberian Pyrite Belt (IPB), in the southwestern Iberian Peninsula, is one of the Earth's largest volcanogenic massive sulfide (VMS) metallogenic provinces [25]. Its long-term and large-scale extraction and processing of metals, since prehistoric times (i.e., the chalcolithic period, ca. 4500 years ago until today [26,27], has left behind a legacy of abandoned mines and on-site pyrite-rich waste material. In that sense, the IPB has been recognized as one of the most polluted places on Earth because of acid mine drainage discharges [28–31]. A specific residue known in the area as "morrongos" was mainly produced during the 19th century when 40–50 Mt of pyritic ore with a low Cu grade (< 3%) was processed for sulfur removal and subsequent Cu extraction by roasting of pyrite followed by artificial cementation [32]. Currently, the "morrongos" mine waste still remains on site in many old and current mines and is being exposed to weathering. As a result, it

is undergoing atmospheric oxidation while releasing emanations that acidify waters with a high risk of contaminating the surface and sub-surface waters connected to the river drainage network. Most of these pyritic residues are not treated, posing a serious threat to the environment and, consequently, to public health and safety. Previous valuable studies in the area have focused mainly on the toxic nature of the "morrongos" residues [33,34], whereas their economic potential for tech metals has been unexplored.

Here, we target the geochemical and mineralogical characterization of a wide suite of metals in these mine wastes by means of a combination of analytical techniques for whole rock analysis (Inductively Coupled Plasma Atomic Emission Spectroscopy (ICP-AES), Inductively Coupled Plasma Mass Spectrometry (ICP-MS), Fire Assay Atomic Absorption Spectrophotometry (FA-AAS), and mineral nano-to-micron scale analysis (Electron Microprobe (EPMA), Laser Ablation Inductively Coupled Plasma Mass Spectrometry (LA-ICP-MS), Field Emission Scanning Electron Microscopy (FE-SEM), and Focused Ion Beam High Resolution Transmission Electron Microscopy (FIB-HRTEM). The present study contributes to a sustainable supply of metals for the ecological transition by means of the first ever estimation for the revalorization and reclassification of these mining residues as possible new resources of tech metals.

2. Contextualization of the Roasted Pyritic Wastes "Morrongos"

2.1. The Massive Sulfide Deposits of the Iberian Pyrite Belt

The Iberian Pyrite Belt is located in the southwestern portion of the Iberian Peninsula (Figure 1). Extending about 250 km from Sevilla province, in SW Spain, to south of Lisbon, Portugal, it groups, within a belt of 40–60 km wide, about 90 volcanogenic massive sulfide (VMS) deposits of polymetallic nature (Cu, Pb, and Zn; [35–37]). Byproducts and trace metals (Au, Ag, Co, Ni, Mn, Cd, In, Sn, Se, Bi, Te, Ga, Ge, Sb, and Ba) are also reported in concentrations ranging from tens to hundreds of ppm [37–42]. The VMS ores mainly consist of pyrite [FeS_2] (>90 vol.%) with variable amounts of other sulfides, including (chalcopyrite [$CuFeS_2$], galena [PbS], sphalerite [(Zn,Fe)S], tennantite-tetrahedrite [$(Cu,Fe)_{12}As_4S_{13}$-$(Cu,Fe)_{12}Sb_4S_{13}$], and arsenopyrite [FeAsS]). Minor mineralogy includes Bi- and Pb-sulfosalts, cassiterite [SnO_2], magnetite [Fe_3O_4], stannite [Cu_2FeSnS_4], electrum [AuAg], and cobaltite [CoAsS]. Ore bodies are mainly hosted by black shales to the south and felsic volcanic and volcaniclastic rocks to the northern part (Figure 1; [36,42]). The economic value of the IPB is mainly concentrated in about 2000 Mt of massive sulfide ore, with several major deposits, including Tharsis (>110 Mt), Massa Valverde (~100 Mt), Aznalcóllar-Los Frailes (~160 Mt), Riotionto (~500 Mt), Neves Corvo (>210 Mt), Aguas Teñidas (>50 Mt), Sotiel-Migollas (~130 Mt), and La Zarza (~170 Mt) [43].

2.2. The Roasted Pyritic Wastes "Morrongos"

As noted in Section 1, "morrongos" is a specific mining waste produced in the IPB during the 19th century as a result of S removal and Cu extraction by pyrite roasting followed by artificial cementation. This pyrite processing usually took place in the vicinity of the mineral extraction areas, when pyrite ore was roasted in special open-air heaps of 100–800 t, known as "teleras". The firing of the pyrite heaps (both conical and prismatic) usually lasts between six and seven months, releasing sulfur dioxide into the atmosphere while leaving behind the so-called "morrongos". These "morrongos" were washed with water in order to lixiviate Cu-sulfate. Then, Cu-sulfate was accumulated in decantation ponds to remove suspension loads and, finally, into "cementation" tanks, from where it circulated through channels (i.e., "canaleos") filled with steel scrap that allowed precipitation of Cu by ionic replacement of the Fe. Cement Cu, named "cáscara", reached grades of 60% to 90% Cu. The consumption of Fe to facilitate Cu precipitation ranged from 1.5 to 3.0 kg per kg of Cu.

The location sites chosen for this study cover different portions of the Odiel river drainage network, which streams north-to-south for 128 km through southern Spain to join the Tinto River and form a common estuary at the town of Huelva (Figure 2). The area has a mean annual rainfall of 630 mm with an effective rainfall of close to 396 mm

(inferred from data recorded during the period 1940–2022). The dry period lasts from April to October. The waste dumps located in the upper part of the drainage network are the septentrional ones at San Telmo (ST), Valdelamusa (V), and Cueva de la Mora (CM), whereas those down south correspond to Tinto Santa Rosa (TSR), Sotiel (S), and Tharsis (TH), respectively (Figures 2 and 3).
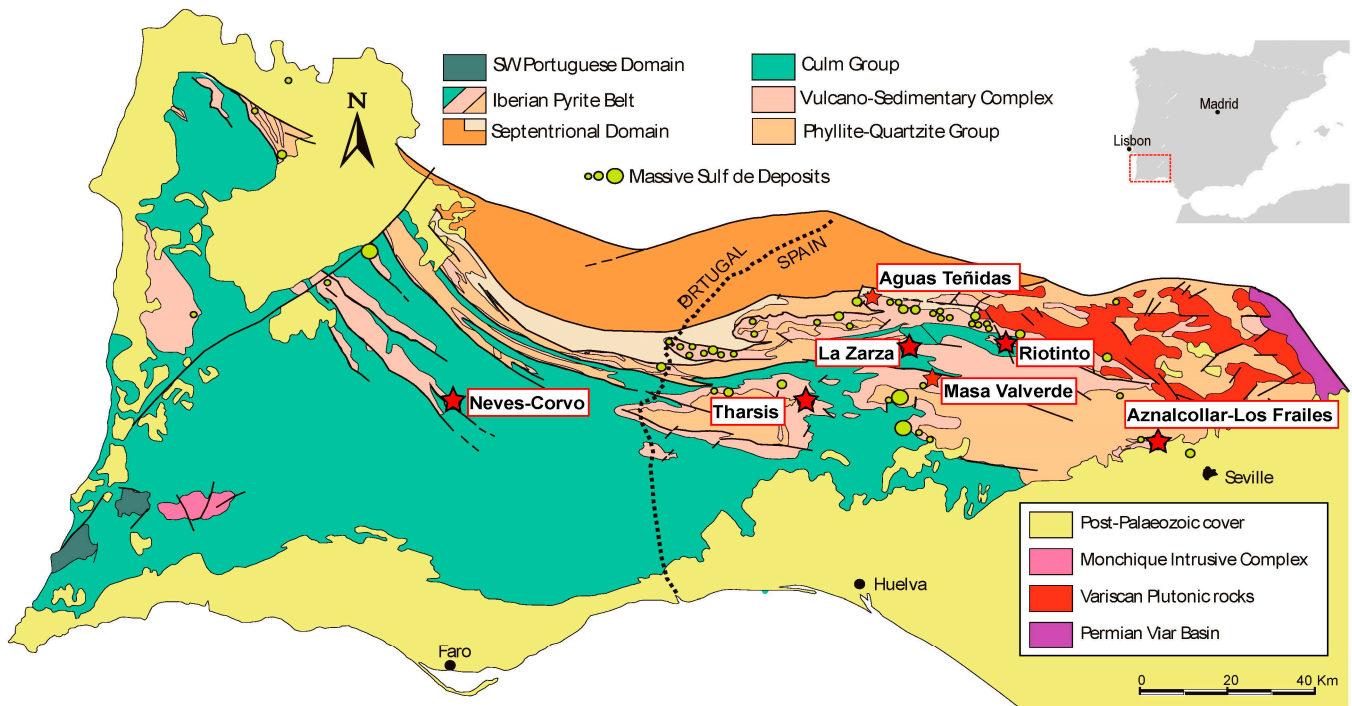

Figure 1. Geographical location of the Iberian Pyrite Belt (IPB) in the geologic frame of south-western Europe (modified from [44]) showing the location of the main VMS exploited in the area.

The waste pile of "morrongos" cropping out near the San Telmo open pit (also known as Santa Bárbara) covers a surface area of 11,578 m^2 and has a maximum thickness of 6 m (Figure 2a). In this stockpile, there are vent chimneys for roasting pyrite, suggesting that this waste dump is still in situ (Figure 3a,b). An unknown portion of the original morrongo stockpile produced during the second half of the 19th century is missing due to the exportation of Cu-depleted "morrongos" as Fe ore in the 1960s [45].

At Valdelamusa, two "morrongos" dumps crop out in the proximities of the homonym locality, covering a total area of 17,525 m^2 with a maximum thickness of 3 m (Figure 2b). These pyritic wastes are not in situ, but they correspond to mixed material coming from the nearby mines of Lomero-Poyatos, San Telmo, Cueva de la Mora, El Carpio, and/or Confesionarios (Figure 3c). This is due to the fact that Valdelamusa was a main railway station where pyrites and mine wastes were stockpiled to be later transported by train to the Port of Huelva (a distance of 67 km) for exportation.

The Cueva de la Mora "morrongos" are located on the riverbank of the Olivargas Creek (Odiel river basin), placed over a slate debris dump (Figure 2c). This waste facility that covers an area of 179,695 m^2 with a maximum thickness of 10 m was identified by the code 1038-1-0004 in the Spanish national inventory of mine and metallurgical waste development by the IGME; this document remarks that those "morrongos" could be valorized [46]. This material comes from a mining operation active since 1875, involving (1) open-air calcinations in "teleras", and (2) a mixture of crushed rich Cu-grade ore with "morrongos" (in the proportion of 1 to 3). This has resulted in places of mixed material made up of "morrongos" with slates and pyrite (Figure 3d,e).
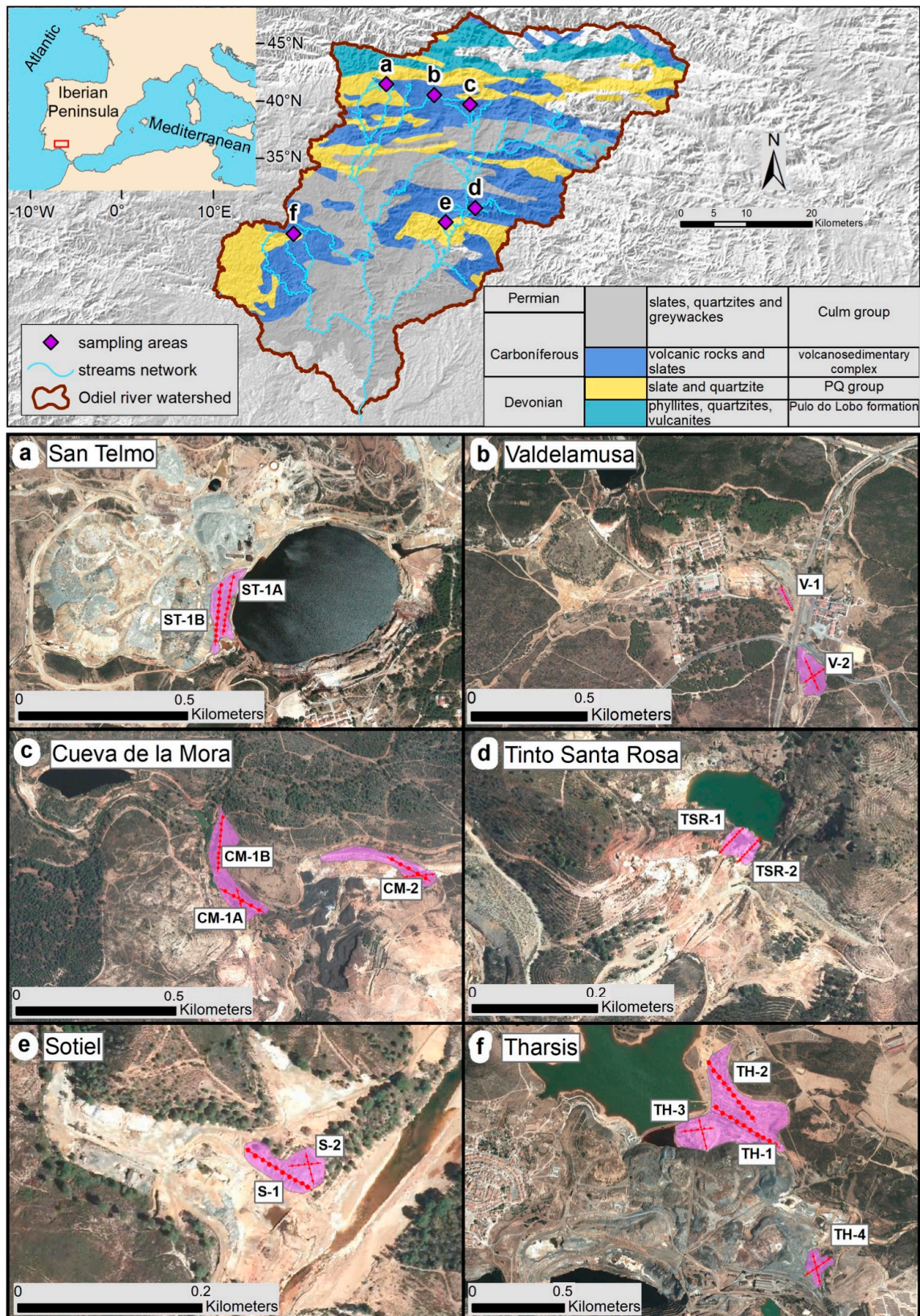
Figure 2. Drainage network of the Odiel river in the geological framework of the IPB in southwestern Spain showing the locations and areal distribution of the roasted pyritic waste "morrongos" targeted in this study (**a–f**).
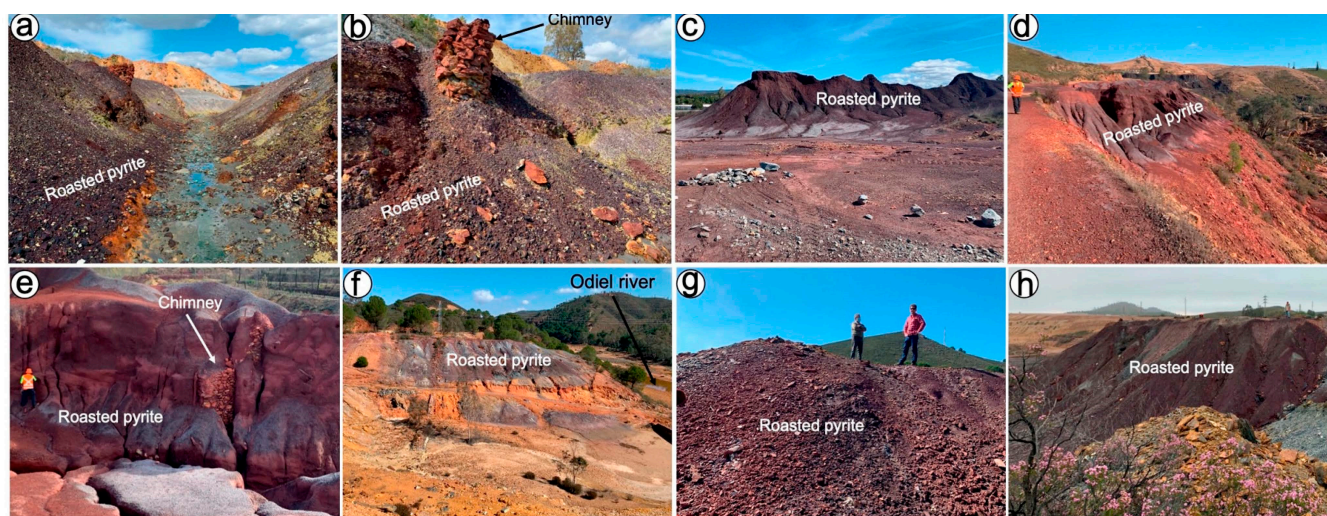
Figure 3. Pictures of open-air pyrite roasting residues ("morrongos") dumps from the 19th century at San Telmo (**a**,**b**), Valdelamusa (**c**), Cueva de la Mora (**d**,**e**), Sotiel (**f**,**g**), and Tharsis (**h**).

The Tinto-Santa Rosa roasted pyrite heap has a surface area of 3123 m^2 and a maximum thickness of 10 m (Figure 2d). These "morrongos" are currently placed next to the Tinto-Santa Rosa open pit mine, were active during the second half of the 19th century due to an attempt to backfill them during the rehabilitation measures that were carried out in the 1990s. Here the "morrongos" may be, in places, also mixed up with other types of mining waste.

The waste dump targeted in Sotiel is unique to this study and was produced by pyrite roasting during the 20th century. It is located near the riverbanks of the Odiel River, and is in its flooding area, covering an area of approximately 4364 m^2 with up to 10 m thickness (Figure 2e). Here, the "morrongos" may also be locally mixed with other types of mining waste (Figure 3f,g). Nevertheless, they are in situ and attest to the identification of some abandoned mining facilities, such as an open-air pyrite roasting heap known as "telera", a "cementation" pond, and channels called "canaleos" where copper was precipitated upon scrap Fe.

The two mine waste dumps studied in the Tharsis mining complex are former "telera" sites (Figure 2f). A significant portion of the "morrongos" produced during the 19th century was leached during the end of the 20th century, attempting to recover precious metals (i.e., Au and Ag) [47,48], thus leaving a stockpile covering an area of 16,317 m^2 with a maximum thickness of 2 m. The original "morrongo" still preserved in situ covers an area of 11,991 m^2 with a maximum thickness of 10 m (Figure 3h).

3. Materials and Methods

3.1. Sampling and Sample Preparation

A sampling network was designed in several profiles parallel to and perpendicular to the waste dumps. The position of the samples was located on the updated to the year 2020 regional orthophotography—0.25 m resolution—from the Andalusian Environmental Information Network [49]. Samples were collected using a polypropylene shovel and subsequently transferred to clean propylene bags and transported to the laboratory. Each one of the samples weighed 1.5–3 kg and was the composite of at least three extractions performed randomly (but separated by at least 1 m) across the vertical of the stock pile. The extraction sites were selected on the basis of changes in the macroscopic appearance of the waste material, taking into account color, texture, and the degree of aggregation. In the laboratory, each of the samples was dried at 60 °C for 48 h, then broken into solid clods and subsequently mixed for homogenization. After this process, 10 grounded sub-samples originally collected in the field from the same locality were reduced to a final subset

of 15 samples, which were subsequently employed for geochemical and mineralogical characterization. Aliquots were also employed to obtain several thin sections, polished thin sections, and cylindrical polished Epoxy® mounts.

3.2. Bulk-Rock Analysis of Major, Minor, and Trace Elements

Major, minor, and trace elements of the selected samples were determined at the MSALABS laboratories (Langley, BC, Canada) using a 4-acid digestion (hydrochloric, nitric, perchloric, and hydrofluoric acids), ICP-AES, and ICP-MS. The compositions of reference materials OREAS-601, MP-1b, and CDN-ME-1407 were analyzed as unknowns during the analytical runs and show good agreement with the working values of these international standards. Au contents were obtained from aliquots of the samples by Fire Assay Atomic Absorption Spectroscopy (FA-AAS). The analyses of the CDN-GS-P8H-certified reference material compared well with the published values of these standards. Results and detection limits are given in Table S1.

3.3. FE-SEM and EPMA

Polished thin sections and mounts were studied firstly under transmitted and reflected light ore microscopy in an effort to preliminary identify minerals and their textural relationships. Minerals of interest were imaged and identified qualitatively by their characteristic Energy Dispersive Spectra (EDS) using two different instruments: a QEMSCAN 650F Field Emission Gun Environmental Scanning Electron Microscope (FEG-ESEM) and a Leo Gemini Field Emission FE-SEM belonging to the Centro de Instrumentación Científica of the Universidad de Granada, Spain. These instruments are equipped with SE, BSE, and EDS detectors. The accelerating voltage was 20 kV, and the beam current was optimized for a sufficient number of counts for each EDS analysis and mapping.

Once identified in the polished thin sections, the major and minor-element compositions of minerals, including silicates, sulfides, oxides, and sulfates, were obtained by wavelength-dispersive spectrometry (WDS) EPMA using a JEOL JXA-8230 at the Centres Científics i Tecnològics of the University of Barcelona (CCiTUB, Barcelona, Spain). An accelerating voltage of 15 keV and a beam current of 20 nA were used. All elements were measured with a counting time of 15 s for the peak. Data are provided in Table S2 for each of the three specific routines designed for the analyses of silicate, oxides, sulfates, and sulfides. Calibration for silicate analyses was performed using natural diopside for SiO_2, kyanite for Al_2O_3, fluorite for F, periclase for MgO, wollastonite for CaO, orthoclase for K_2O, rhodonite for Mn, rutile for TiO_2, and synthetic albite for Na_2O, AgCl for Cl, and Fe_2O_3 for FeO; the X-ray lines employed were Kα for all the analyzed elements. The standards used for the analyses of oxides and sulfates included natural kyanite for Al_2O_3, periclase for MgO, albite for Na_2O, rutile for TiO_2, orthoclase for K_2O, barite for SO_3, rhodonite for MnO, chalcopyrite for CuO, and sphalerite for ZnO, synthetic GaAs for As_2O_5, Fe_2O_3 for Fe, PbS for PbO, and HgS for HgO, and metallic Sb for Sb_2O_5, Ag for Ag_2O, and Au for Au_2O. The X-ray lines employed Kα for Al, Mg, Na, Ti, K, Fe, Mn, Cu, Zn, and S, Lα for Sb, Au, and Ag, and Lβ for As, Mα for Pb, and Mβ for Pb. For sulfide analyses, we employed the following calibration natural standards: FeS_2 for S and Fe, PbS for Pb, chalcopyrite for Cu, sphalerite for Zn, and the synthetic HgS for Hg, In_2Se for In and Se, GaAs for As, CdS for Cd, metallic Co for Co, metallic Ni for Ni, Au for Au, Ag for Ag, Sb for Sb, and Bi for Bi. The X-ray lines employed were Kα for S, Se, Fe, Co, Ni, Cu, and Zn, Kβ for As, Mα for Pb, Hg, and Bi, and Lα for Ag, In, Cd, Sb, and Au. The results of EPMA are provided in Table S2.

3.4. FIB-HRTEM

Thin-foil samples from oxide-silicate, amenable for examination under transmission electron microscopy (TEM), were prepared using a Dual Beam FEI Thermo-Fisher Scientific Helios 650 belonging to the Laboratorio de Microscopías Avanzadas at the Instituto de Nanociencia de Aragón (INA)—University of Zaragoza, Spain. The chosen locations of

interest were in a first stage covered by protective thin strips of C of ~300 nm thickness and Pt of ~1 μm thickness. Soon after, the bulk material was first removed on both sides of the lamella by rough Ga ion milling with a 30 kV current at 2.5 nA and was subsequently polished with a 30 kV current at 0.23 nA. The final polishing step was performed on thin foil in order to achieve electron transparency. This was completed by subsequently milling the thin foil with a 5 kV current at 68 pA. The electron transparency was monitored with an Everhart-Thornley SE detector using a 5 kV electron beam. After achieving electron transparency, the thin foil was rapidly polished using a low-energy 5 kV current at 10 pA to reduce the amorphization until a final thin foil thickness of ~90 nm was attained. Subsequently, the thin foil was undercut with a 30 kV at 2.5 nA current, lifted out, and transferred from the sample to a TEM grid using an OmniProbe nanomanipulator with a tungsten tip. Ion beam-assisted Pt deposition was used to weld the thin foil to the tungsten tip and the TEM grid.

The thin foils were subsequently analyzed by means of a FEI Titan G2 TEM equipped with a field emission gun (XFEG) belonging to the Centro de Instrumentation Científica of the University of Granada, Spain. This microscope is corrected for spherical aberrance in the objective lens and is also equipped with four energy dispersive X-ray (EDX) detectors (FEI microanalysis Super X) and a high-angle annular dark field detector (HAADF). The thin foils were inspected in this instrument at 300 kV while a Gatan CCD Camera was employed to acquire high magnification electron microscopy images (HMEM) and HRTEM. Selected mineral areas of interest sampled within the thin foil were then imaged and chemically characterized using a combination of EDX elemental maps, HAADF (to obtain Z high contrast images), HMEM (to characterize the texture of the grains), and HRTEM (to properly define the ordering of the mineral aggregates). All these images were treated using Digital Micrograph software (version 1.71.38), while the maps were processed with the INCAt Microanalysis Suite (version 4.09) software package.

3.5. In Situ Analysis of Minor and Trace Elements in Minerals by LA-ICP-MS

In situ analyses of minor and trace elements in oxides (i.e., magnetite and hematite) and silicates were obtained by means of LA-ICP-MS on polished mounts at LabMaTer, Université du Québec à Chicoutimi (UQAC) (Table S3). The LA-ICP-MS instrument used was a Thermo X7 ICP-MS with a high-performance interface coupled with a New Wave Research 213 nm Nd: YAG UV laser ablation microprobe. Ablated material was carried by a He–Ar gas mixture and analyzed using the Thermo X7 ICP-MS operating in time-resolved mode using peak jumping. The analyses were conducted using a 10-μm spot diameter, a 25-Hz frequency, a 7 J/cm^2 fluence for oxides, a 15-Hz frequency, and a 6 J/cm^2 for silicates during a 60-s analysis (~30 s for the gas blank and ~30 s for the signal). All data were reduced using Iolite v4 software and by subtracting the gas blank from each of the isotopes analyzed. The instrument was calibrated against the certified reference material GSE-1g for all elements. Fe and Si values obtained by EPMA were used as internal standards for the calibration of oxides and silicates, respectively.

The analyses of oxides were focused on the isotopes ^{24}Mg, ^{27}Al, ^{51}V, ^{29}Si, ^{45}Sc, ^{49}Ti, ^{51}V, ^{55}Mn, ^{59}Co, ^{60}Ni, ^{63}Cu, ^{66}Zn, ^{71}Ga, ^{73}Ge, ^{75}As, ^{107}Ag, ^{111}Cd, ^{118}Sn, ^{121}Sb, ^{125}Te, ^{197}Au, ^{208}Pb, and ^{209}Bi. Si, K, Au, Sn, Ag, and Pb were monitored to check for the presence of solid mineral inclusions. The certified reference materials NIST610, GProbe15, and MASS1, as well as the in-house M1A were analyzed as unknowns during each analytical run to check the accuracy and precision of the analyses. The analysis of reference material (NIST610 and GProbe-15) shows that the accuracy and precision are <15% RD and RSD, respectively, for most elements except for some trace elements, which are heterogeneously distributed within the sample. The in-house M1A and the reference material MASS-1 exhibit higher variations in RD but maintain good RSD for most elements (Table S3). The analyses of silicates monitored ^{24}Mg, ^{27}Al, ^{45}Sc, ^{49}Ti, ^{51}V, ^{55}Mn, ^{59}Co, ^{66}Zn, ^{69}Ga, ^{75}As, ^{85}Rb, ^{88}Sr, ^{208}Pb, and ^{209}Bi. The accuracy and precision of the certified reference materials NIST610,

NIST612, MASS-1, and GProbe-6 are <15% for most elements except for some trace elements (Table S3).

4. Results

4.1. Whole-Rock Distribution of Major, Minor, and Trace Elements

Iron is the major constituent of the roasted pyrite wastes (37 to 50%), followed by sulfur (<5%), and other less abundant lithophile elements such as Al (<4%), K (2%), Ti (<1%), Mg (<0.2%), Na (<0.2%), and Ca (<0.1%) (Figure 4a and Table S1). The two mixed samples from Sotiel (S-2) and Tinto-Santa Rosa (TSR-2) show significantly lower Fe values (13%), but higher sulfur values (up to 10%) (Figure 4a and Table S1).
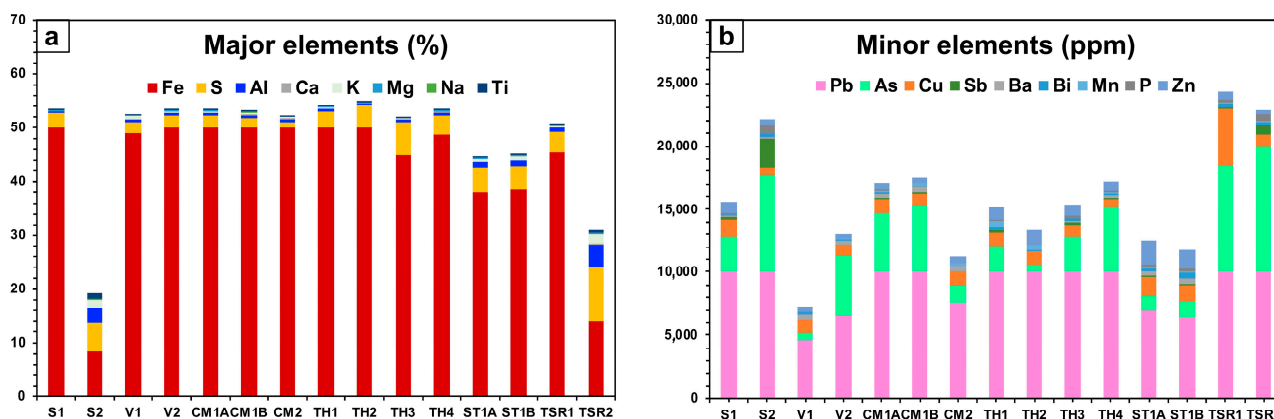

Figure 4. Bulk-rock distribution of major (**a**) and minor (**b**) elements in the analyzed samples.

Metals of economic interest are, in order of abundance, Pb, As, Cu, and, to a lesser extent, Zn, Sb, Ba,Bi, P, and Mn (Figure 4b and Table S1). Pb, As, Cu, and Zn are detected in the average range of thousands of ppm, whereas Sb, Ba, Bi, P, and Mn are below 300 ppm.

Trace elements detected in the range of 10 ppm include, in order of abundance, Se, Sr, Sn, Zr, Tl, Mo, V, Ce, Co, Rb, La, and Cr (Figure 5a and Table S1). In contrast, ultratrace elements detected in proportions below 10 ppm include, in order of abundance, In, Ni, Ga, Y, Th, W, Nb, U, Li, Sc, Te, Cd, Hf, Cs, Ta, and Be (Figure 5a and Table S1).
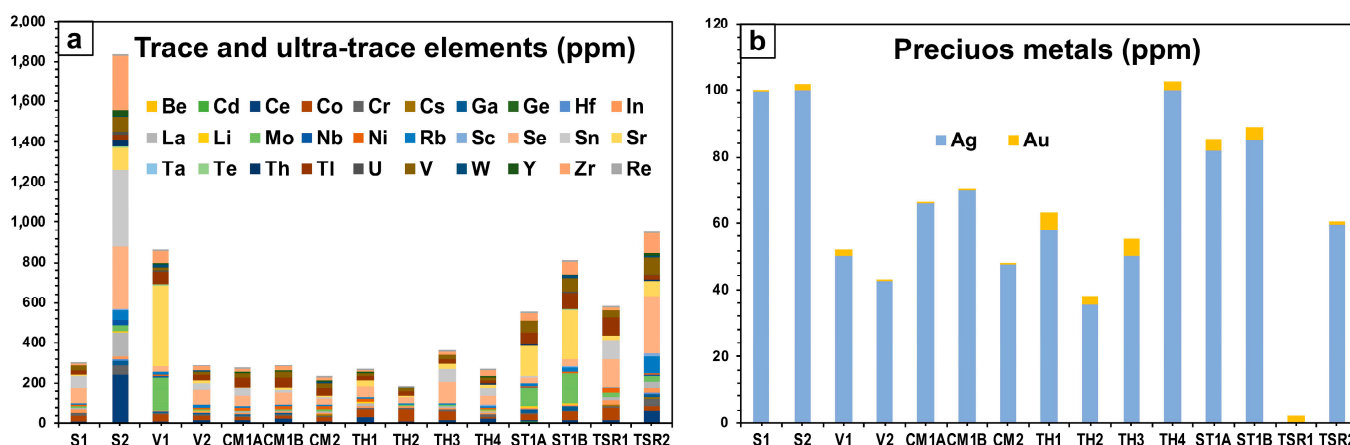

Figure 5. Bulk-rock distribution of trace and ultra-trace elements (**a**) and precious metals (**b**) in the analyzed samples.

All analyzed samples but one (i.e., Tinto-Santa Rosa-1 (TSR1)) have appreciable contents of Ag (35–100 ppm) and Au (2 ppm on average). It is worth noting that the highest Au contents (up to 5 ppm) were detected in the Tharsis-1 (TH-1) sample (Figure 5b and Table S1).

4.2. Mineralogy

Oxides of the spinel group, including magnetite (Fe_3O_4), hematite (Fe_2O_3), and hercynite ($FeAl_2O_4$), are the most abundant minerals in all the samples (Figures 6 and 7). Other less abundant minerals (Figure 7) are sulfates [jarosite, $KFe_3(SO_4)_2(OH)_6$; plumbojarosite, $PbFe_6(SO_4)_4(OH)_{12}$; anglesite ($PbSO_4$) and barite ($BaSO_4$)], arsenates [beudandite $PbFe_3(AsO_4)(SO_4)(OH)_6$], sulfides [galena (PbS), pyrite (FeS_2) and tetrahedrite ($Cu,Fe)_{12}Sb_4S_{13}$], and native metals [Pb^0, Cu^0, Bi^0 and Au^0]. Quartz is also relatively abundant, in addition to trace amounts.

The Fe-oxides of the spinel group frequently form composite aggregates with/without Si-(Al)-rich glass (hereafter pellets) (Figure 6a–l). These pellets, which may be up to 0.5 mm across, exhibit a range of morphologies from purely spheroidal or droplet-like to holly-leaf, with characteristic heterometric internal porosity (Figures 6a–l and 7a–e). Some of the pellets consisting of porous hercynite or magnetite are usually replaced by hematite along their rims (Figure 7a–c).
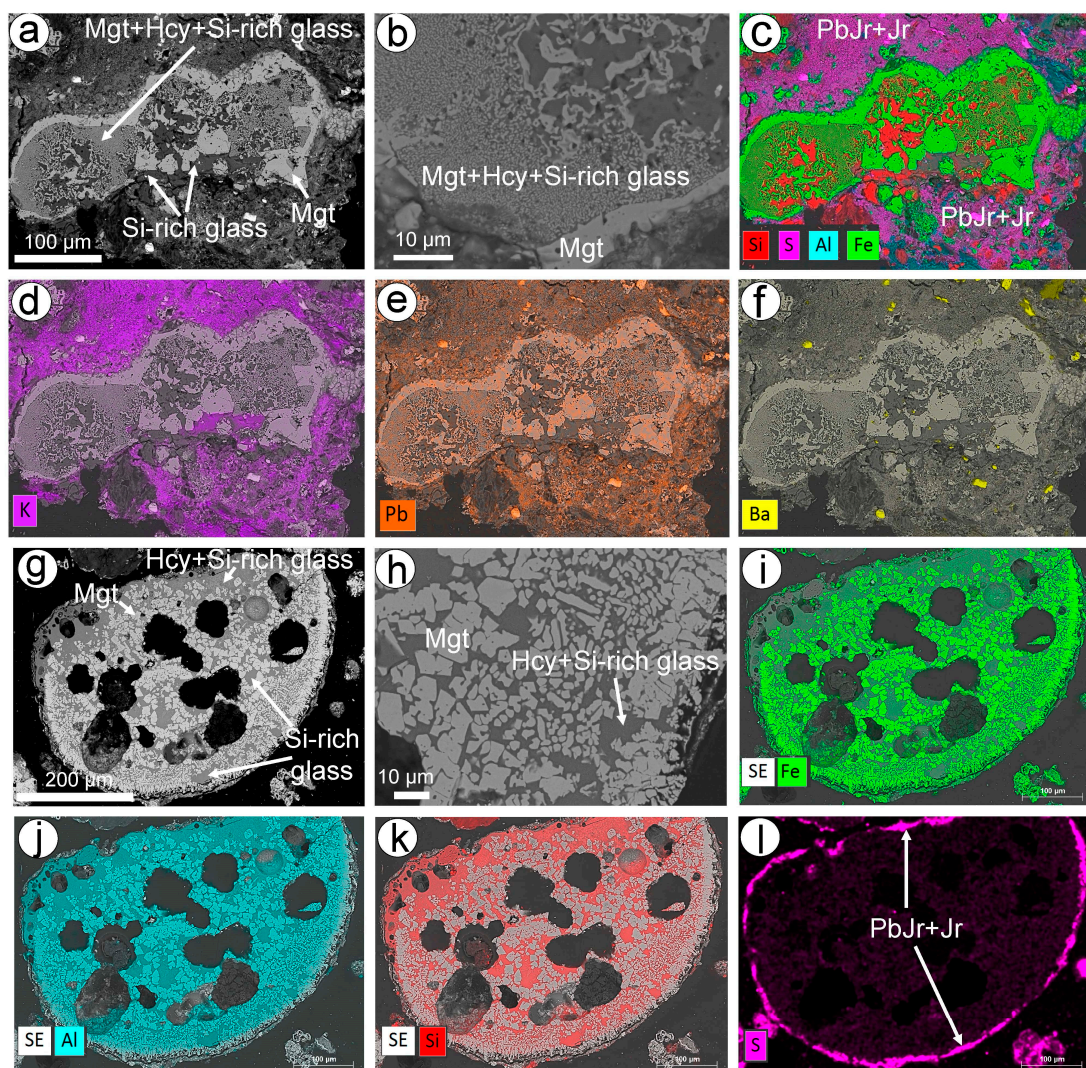

Figure 6. Back-scattered electron images of selected pellets made up of oxide-silicate glass mixtures resulting from the oxidation of pyrite during firing. Note the rounded and lobate external morphology of the aggregates as well as the complex intergrowth of the oxides hercynite and magnetite and the silicate ground mass. The examples come from San Telmo ((**a**–**f**); sample STA-1), ((**g**–**l**); sample CM-2). Keys for acronyms: Hcy (hercynite), Mgt (magnetite), Hmt (hematite), PbJr (plumbojarosite), Jr (jarosite).
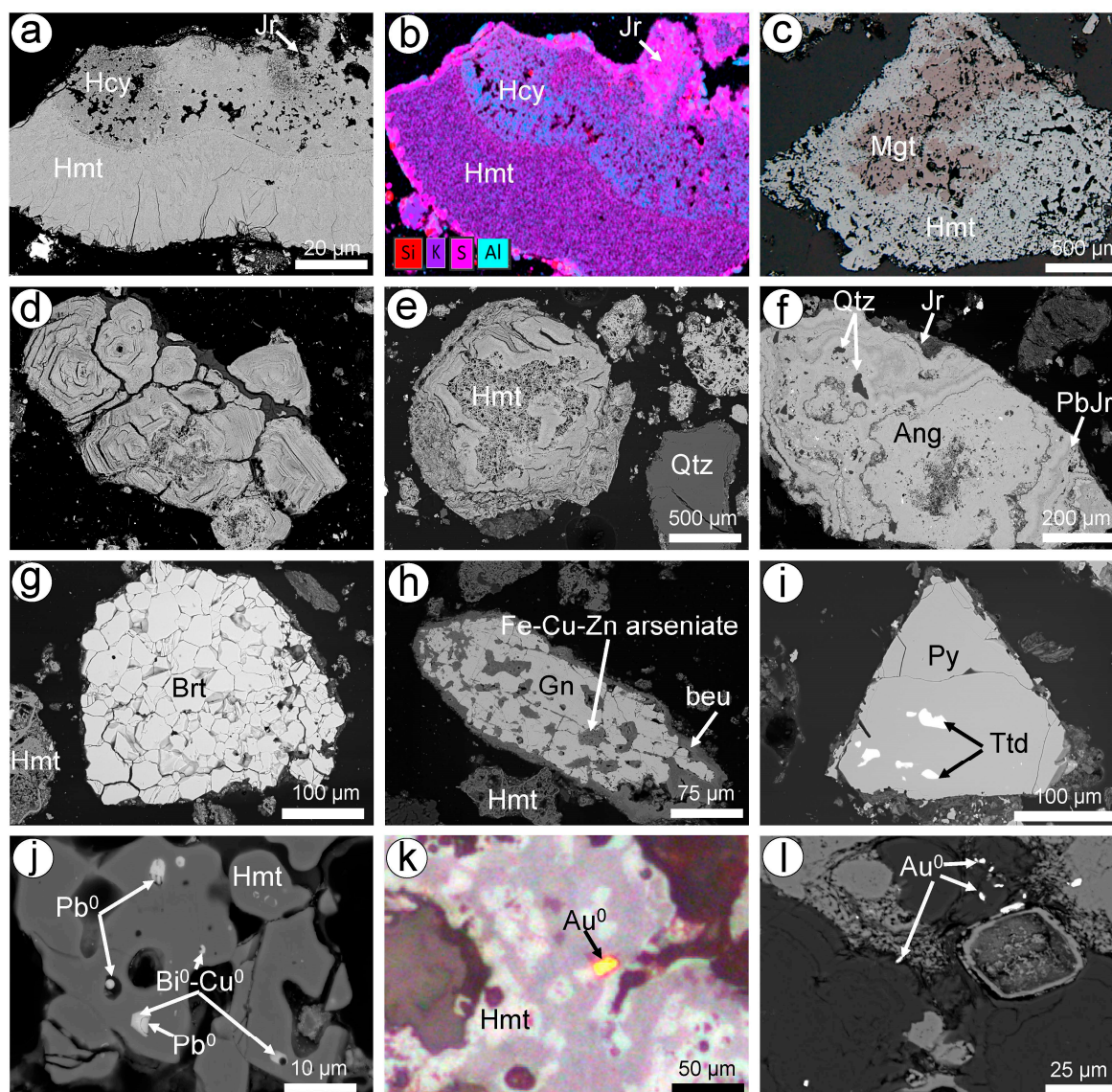
Figure 7. Reflected light microscope and back-scattered electron images of representative minerals accompanying the oxide-silicate mixtures in the studied pyritic residues. (**a**,**b**) A fragment of hercynite replaced by Al-rich hematite from Cueva de la Mora (sample CM-2); (**c**) magnetite replaced by hematite from Tinto Santa Rosa (TSR-1); (**d**,**e**) onion-like internal morphology in hematite pseudomorph after pyrite from San Telmo (sample ST-1B); (**f**) complex aggregate of secondary intergrowth of anglesite and plumbojarosite hosting inclusions of quartz from Tinto Santa Rosa (sample TSR-2); (**g**) isolated aggregate of barite from Valdelamusa (sample V-1); (**h**) broken fragment of galena partly replaced by an unidentified Fe-Cu-Zn arseniate and beudantite from Cueva de la Mora (sample CM-1B); (**i**) broken fragment of unroasted pyrite hosting tetrahedrite from Tinto Santa Rosa (sample TSR-2); (**j**) hematite pseudomorph after pyrite hosting inclusions of native Pb and Bi-Cu amalgams, from Tharsis (sample TH-3); (**k**,**l**) gold particles in samples from Tharsis. Keys for acronyms: Hcy (hercynite), Hmt (hematite), PbJr (plumbojarosite), Jr (jarosite), Qtz (quartz), Au^0 (gold), Gn (galena), Beu (Beudantite), Ang (anglesite), Brt (barite), Py (pyrite), Ttd (tetrahedrite), Pb^0 (native Pb^0), and Bi^0-Cu^0 (Bi-Cu amalgamas).

Sulfates of the jarosite group, including jarosite and plumbojarosite, appear as fine-grained aggregates coating the pellets or as ground masses enclosing fragments of pellets (Figures 6a,c,l and 7a,b). Anglesite forms millimeter-sized colloforms with alternating bands of plumbojarosite (Figure 7f). Barite is found as isolated granular grains (Figure 7g).

Sulfides and sulfosalts distinctive of the primary mineralization include pyrite, galena, and tetrahedrite. These occur as a remnant, mostly embedded, and are replaced along their rims by the aforementioned sulfates (including beudantite) and/or unidentified Fe-Cu-Zn arsenates (Figure 7h,i).

Native metals such as Pb^0, Au^0, and Cu^0-Bi^0 amalgams have also been recognized (Figure 7j–l). Pb^0 occurs as less than 3-μm drop-like grains overgrown by euhedral Cu^0-Bi^0 amalgams, both enclosed in hematite (Figure 7j). Native Au and electrum form single particles (up to 25 μm) embedded within porous hematite (Figure 7k) or as isolated grains (Figure 7l).

When inspected under high magnification of FESEM, the Fe-oxides immersed in the silicate glass of the pellets display a range of sizes and shapes, including micrometric-sized myrmekite-like and mosaic-like arrangements to dendritic and arborescent intergrowths, as well as single needles and plates consisting of crystals <1 μm (Figures 8 and 9). The FIB-HRTEM observation of the thin foil cut along the contact of myrmekite-like oxides and the silicate glass groundmass from San Telmo (thin-foil #1 in Figure 8), confirms the crystallinity of the oxides and the amorphous nature of the Si-(Al)-rich vitreous groundmass (see images a–d shown in Figure 8).
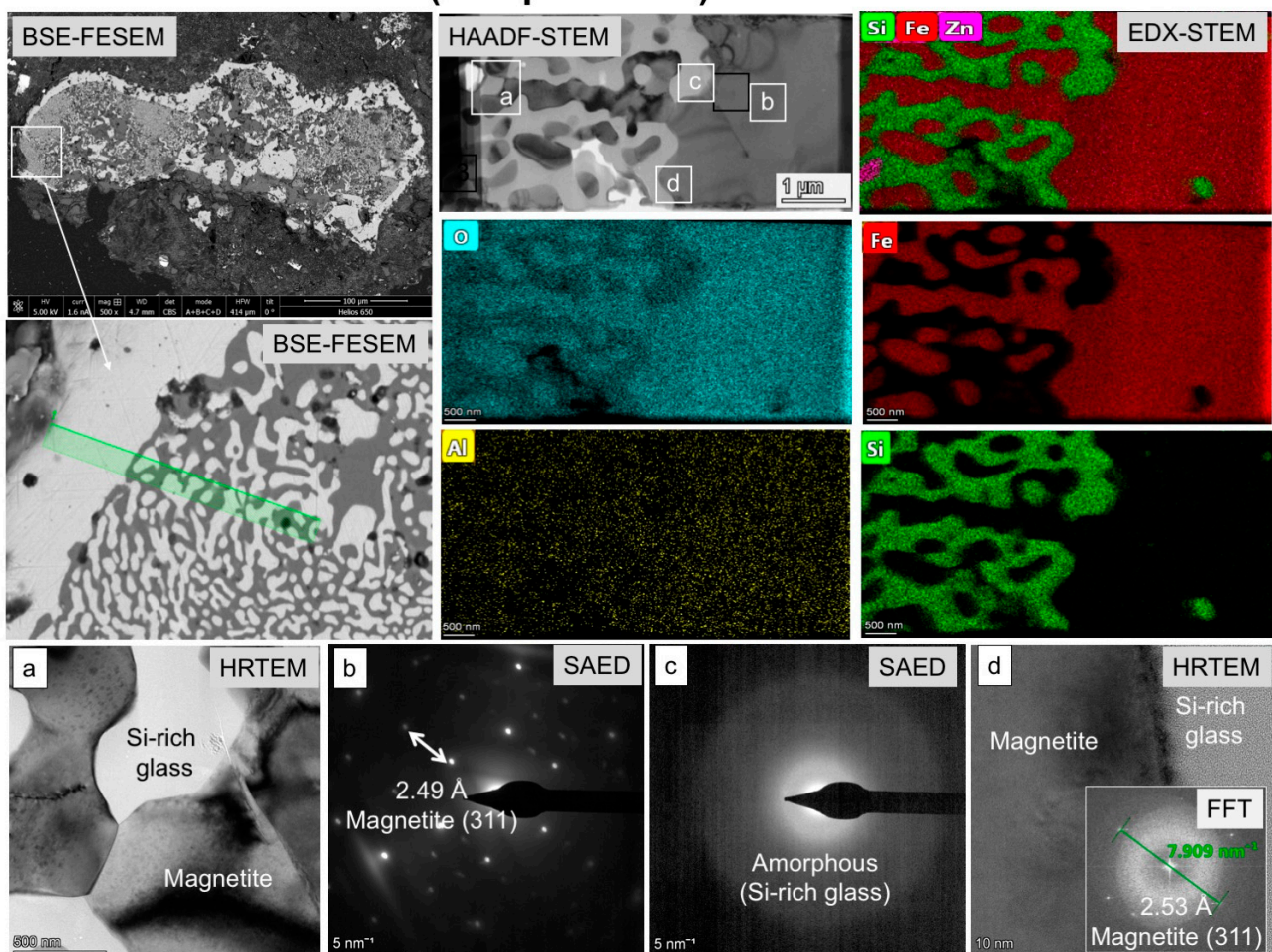

Figure 8. Characterization by a combination of FIB and HRTEM of a thin foil extracted from selected oxide-silicate glass mixtures from San Telmo (thin-foil #1 sample ST-1A). Legends of the technique employed are inset in the corresponding image (see details in the main text) whilst location of the thin foil in the selected samples is marked by a green dotted square).

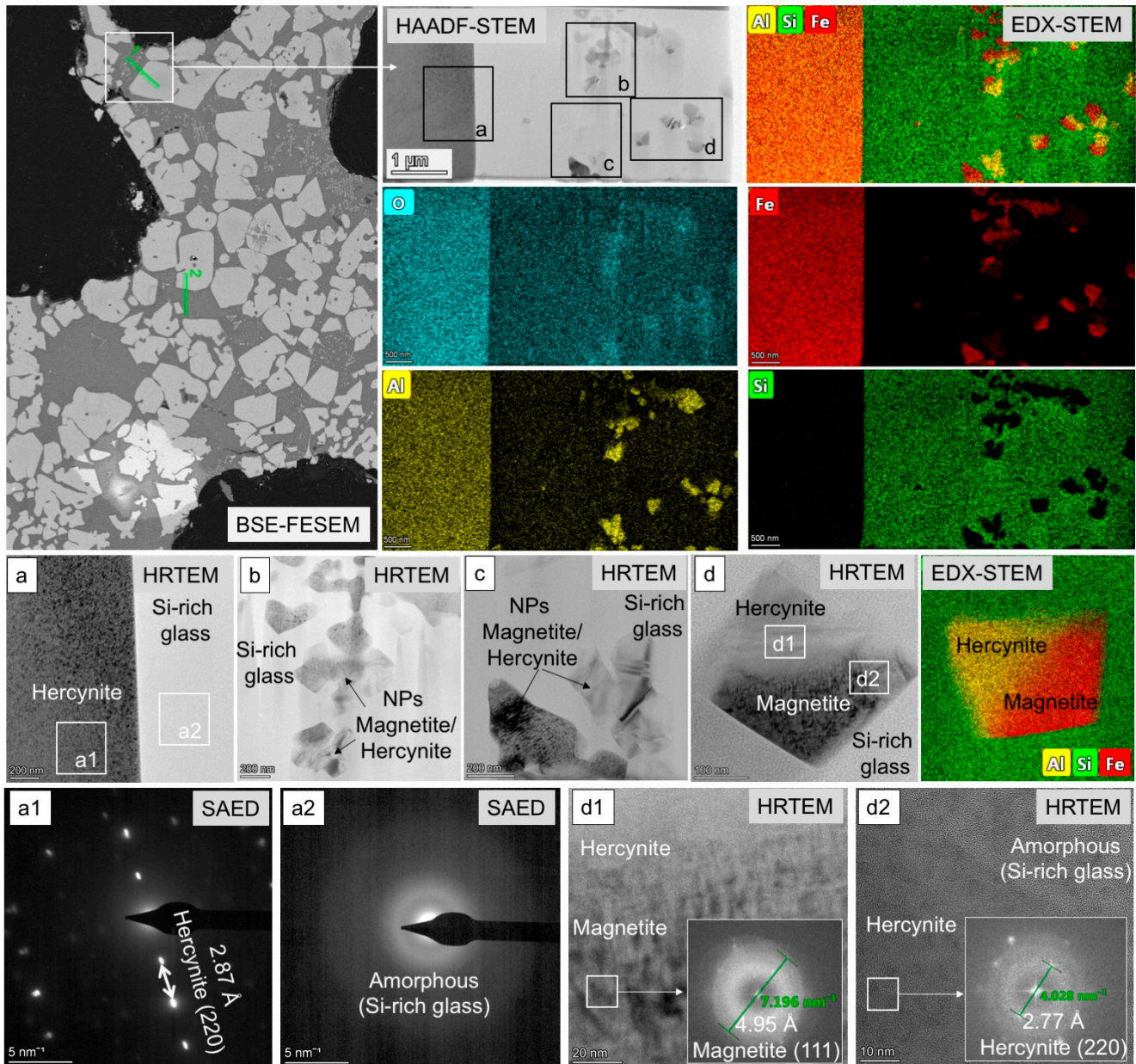# Thin-foil #2 Cueva de la Mora (Sample CM-2)

Figure 9. Characterization by a combination of FIB and HRTEM of two thin foils extracted from selected oxide-silicate glass mixtures from Cueva de la Mora (thin-foil #2 upper images and #3 lower images; sample CM-2). Legends of the technique employed are inset in the corresponding image (see details in the main text) whilst location of the thin foil in the selected samples is marked by a green dotted square).

The FIB-HRTEM observation of the thin foils cut along the mosaic-like (oxides and silicate glass) pellet from Cueva de la Mora also shows crystalline oxides immersed in an amorphous Si-(Al)-rich vitreous groundmass (e.g., images a1–d2 in thin-foil #1 shown in Figure 9). In addition, HRTEM observation of the skeletal and arborescent arrangements reveals a plethora of micron-to-nano-sized crystals of hercynite and magnetite found both isolated or mutually intergrown within the silicate glass (e.g., images a–d in thin-foils #1 shown in Figure 9).

4.3. Mineral Chemistry

In addition, 140 EPMA and 65 LA-ICP-MS analyses were carried out on selected grains of the mineral assemblage forming the "morrongos" (Tables S2 and S3, and shown in Figures 10–14).
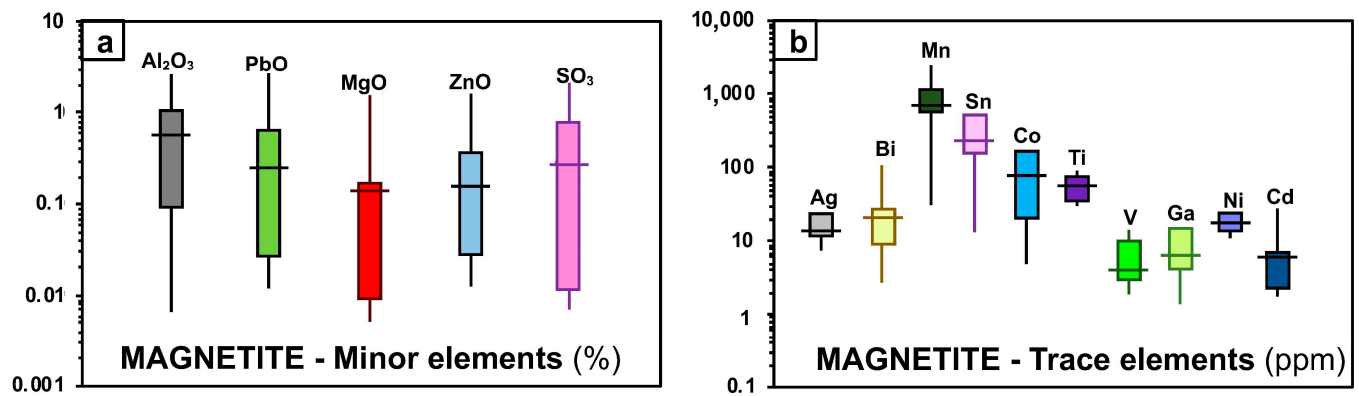

Figure 10. Box diagrams showing major, minor, and trace elements detected in magnetite by means of EPMA (**a**) and LA-ICP-MS (**b**).

Figure 11. Box diagrams showing major, minor, and trace elements detected in hematite by means of EPMA (**a**) and LA-ICP-MS (**b**).

Figure 12. Box diagrams showing major, minor, and trace elements detected in glass by means of EPMA (**a**) and LA-ICP-MS (**b**).
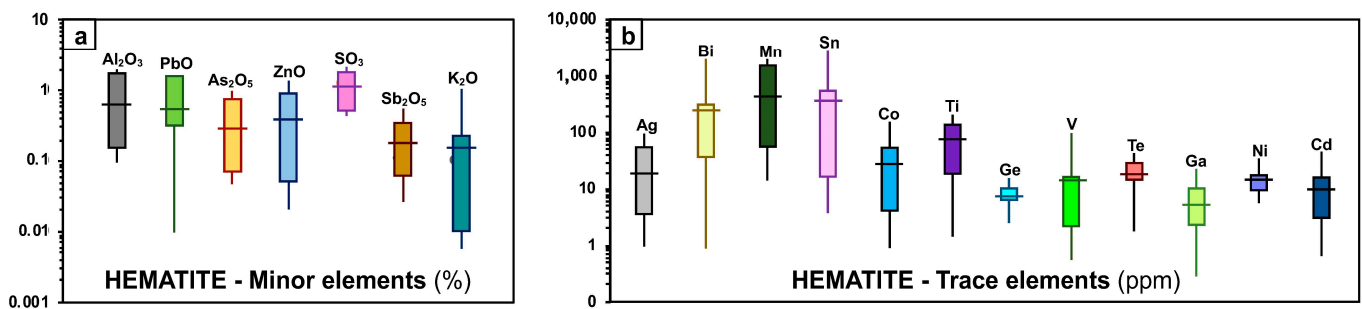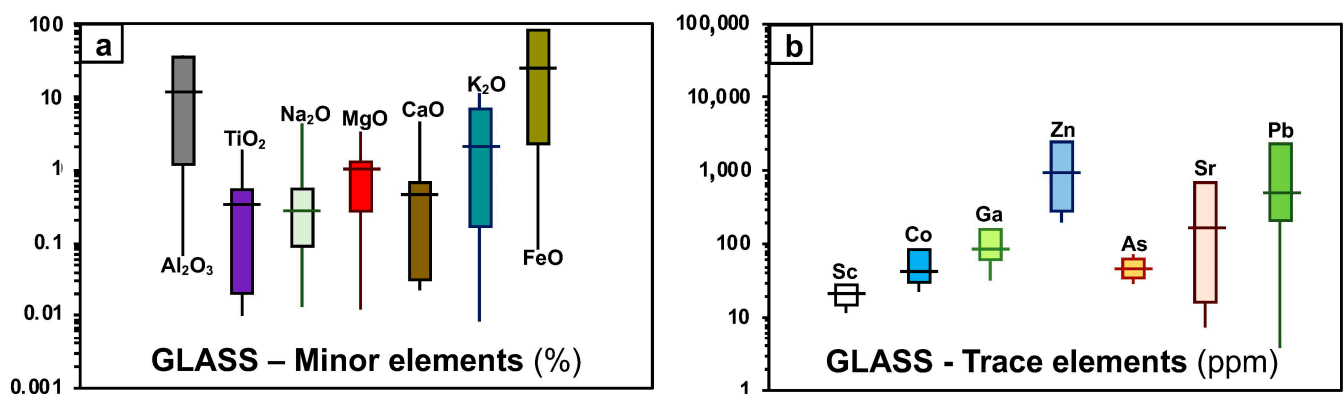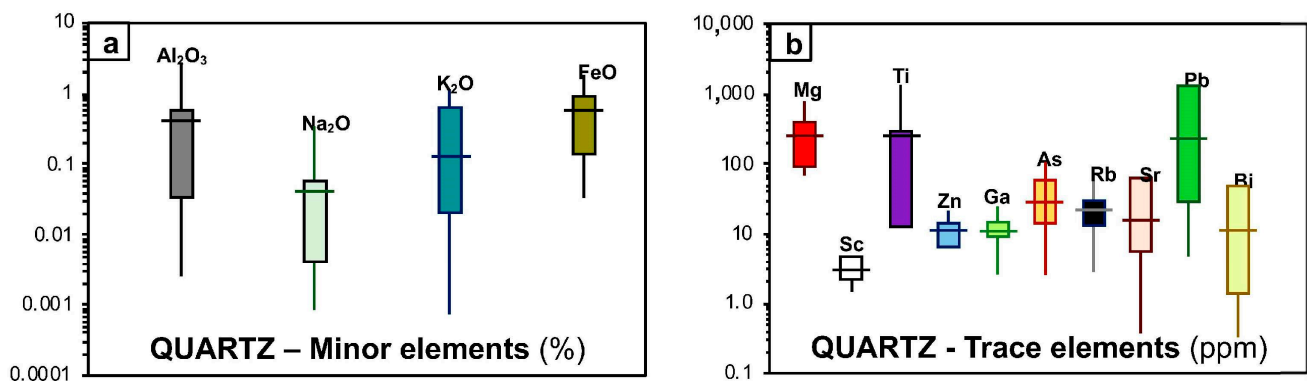
Figure 13. Box diagrams showing major, minor, and trace elements detected in quartz by means of EPMA (**a**) and LA-ICP-MS (**b**).
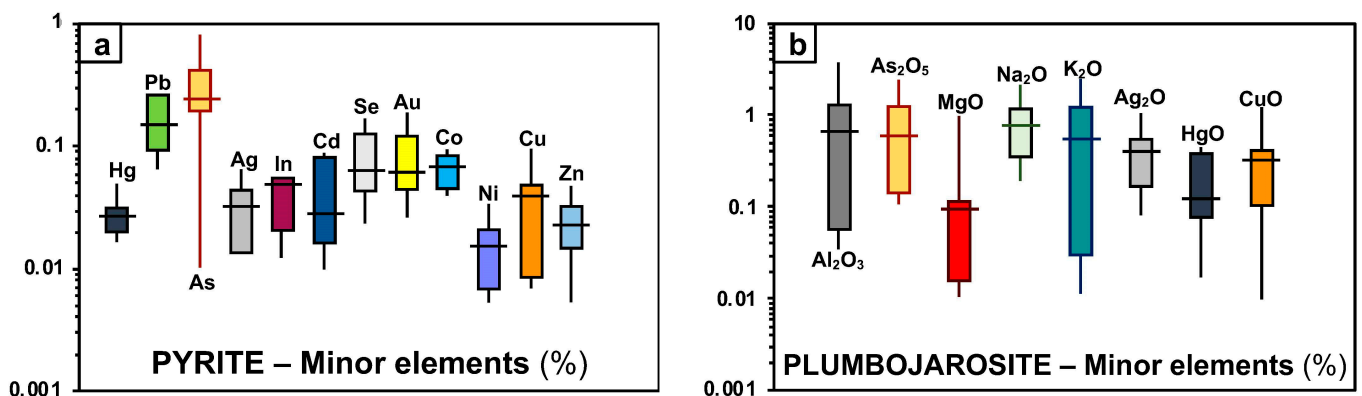

Figure 14. Box diagrams showing minor elements detected in pyrite (**a**) and plumbojarosita (**b**) by means of EPMA.

4.3.1. Oxides

The chemistry of magnetite is relatively homogenous among grains from a single sample, as well as among samples from the different localities studied here (Tables S2 and S3). The analyzed grains show up to 2.5 wt.% Al_2O_3 and 1.3 wt.% MgO, as well as 1.85 wt.% SO_3, 2.5 wt.% PbO, and 1.4 wt.% ZnO, which are very likely related to the nano-to-micron inclusion of sulfates and sulfides eventually included in magnetite (Figure 10a). In situ LA-ICP-MS analyses show relative average enrichment in Mn (~725 ppm), Sn (~140 ppm), Co (~76 ppm), and Cu (~1003 ppm), but depletion in V, Ni, Ag, and Au (Figure 10b).

Hematite contains detectable amounts of Al_2O_3 (up to 1.75 wt.%), PbO (up to 1.41 wt.%), ZnO (up to 1.25 wt.%), As_2O_5 (up to 0.8 wt.%), Sb_2O_5 (up to 0.5 wt%), and K_2O (up to 0.93 wt.%) (Figure 11a and Table S2). The latter elements are very likely related to inclusions of sulfates, arsenates, and sulfides. The LA-ICP-MS analyses detected averages of hundreds to a few ppm of other metals such as Cu (457 ppm), Mn (355 ppm), Mg (288 ppm), Sn (286 ppm), Bi (173 ppm), and Co (27 ppm). Other metals, including Ge, V, Te, Ga, Ni, and Cd, are detected in amounts below 10 ppm (Figure 11b and Table S3).

Hercynite is nearly stoichiometric, although it still contains appreciable amounts of MgO (up to 0.5 wt.%) and TiO_2 (0.33 wt.%) (Table S2). Remarkable average amounts of minor and trace elements detected by LA-ICP-MS are 3896 ppm Zn, 2609 ppm As, 1120 ppm Pb, 741 ppm Mn, and 407 ppm Cu (Table S3).

Minium is enriched in As_2O_5 (up to 0.5 wt.%), Al_2O_3 (0.34 wt.%), and HgO (0.2 wt.%) (Supplementary Table S2).

4.3.2. Silicates

The silicate glass forming the pellets is characterized by an average high of SiO_2 (88.4 wt.%), Al_2O_3 (32 wt.%), and K_2O (9.86 wt.%), but low MgO (2.88 wt.%), TiO_2 (2 wt.%), CaO (4.07 wt.%), and Na_2O (3.78 wt.%) (Figure 12a). Other metals of economic interest detected by means of LA-ICP-MS include Zr (151 ppm on average), Sr (30 ppm on average), and Pb (145 ppm on average) (Figure 12b).

Quartz shows a homogenous composition in terms of major elements (Figure 13a and Table S2), being characterized by its depletion in most of the analyzed elements except Ti (30,291 ppm on average), Pb (1025 on average), and Mg (614 on average) (Figure 13b and Table S3).

4.3.3. Sulfides

The EPMA analyses on selected pyrite grains show relatively low concentrations in most metals of economic interest (<0.1 wt.%), but As (up to 0.84 wt.%) and Pb (0.27 wt.%) (Figure 14a and Table S2).

4.3.4. Sulfates

Plumbojarosite has a very homogenous composition, although some grains contain detectable amounts of Al_2O_3 (up to 3.69 wt.%), As_2O_5 (2.5 wt.%), Na_2O (2 wt.%), K_2O (2.4 wt.%), Ag_2O (1 wt.%), HgO (0.43 wt.%), and CuO (1.16 wt.%), very likely due to the presence of inclusions (Figure 14b). Likewise, anglesite shows a composition nearly stoichiometric (Table S2).

5. Discussion

### 5.1. Genesis of the "Morrongos" during Pyrite Roasting and Later Evolution

The mineralogy, morphology, and internal microstructures of the pellets identified in the studied "morrongos" (Figures 6a–l, 7a–e, 8 and 9) are similar to those resulting from the roasting and/or calcination processes of pyrite as documented in both natural settings and experimental runs [50–52]. The nano-to-micron-sized structures consisting of mixtures of hercynite, magnetite, and/or hematite and silicate glass shown by our pellets are consistent with (1) cooling from a melted mass; and (2) decomposition, upon cooling, of a precursor high-temperature spinel phase.

Experiments conducted at a high temperature (1200 °C) indicate that the Fe-Al end-member spinel hercynite may dissolve up to 16.5 wt.% of the magnetite component in its structure while releasing it upon decreasing temperature and/or increasing oxygen content [53,54]. Furthermore, the replacement textures of hercynite and magnetite by hematite (Figure 7a–c) are consistent with the progressive oxidation sequence of pyrite → hercynite/magnetite → hematite that is typically produced during combustion of pyrite in oxygen-containing atmospheres, particularly when Al-bearing silicates are present in the gangue of the pyrite ore subjected to combustion [51].

The proposed sequence of decomposition of pyrite to hercynite, and then magnetite and/or hematite, usually left behind by the latter oxides enriched in Al (i.e., up to 12.13 mol.% of Al_2O_3), has been detected in these types of oxides synthetized at 1200 °C. This is consistent with the fact that the newly formed Fe-oxides analyzed here show relatively high Al_2O_3 contents (up to ~52 wt.% in hercynite, ~2.5 wt.% in magnetite, and ~1.8 wt.% in hematite; Figures 10 and 11 and Table S2), evidencing the contribution of Al-rich phases during pyrite combustion. It is worth noting that phyllosilicates such as chlorite and sericite were the main gangue minerals of the pyritic ores employed for the roasting process [36,55], thus providing a potential source for Al in the newly formed minerals. The thermal stability of these hydrate-minerals is <600 °C [56], which is far below the temperatures reached during the firing of pyrite in the study area. For instance, Ref. [32] experimentally tested that mineralogical decomposition of pyrite during roasting in the nearby Riotinto "Teleras", where the "morrongos" residues were produced, could

have reached up to 600 °C during firing with oxidation and phase transition of pyrite into Fe-oxides at >900 °C, consistent with estimations made here.

Additionally, we have also observed the replacement magnetite → hematite, both lacking Al (Figure 7c). This raises another possible pathway during firing, where pyrite decomposes to those Fe-oxides without the necessity of a hercynite precursor. A possibility is the two-stage processes observed by [52] in their experiments conducted at 500–700 °C, where pyrite is firstly oxidized to magnetite and the latter to hematite upon increasing oxygen fugacity, according to the following reactions:

$$3FeS_2 + 16O_2 \rightarrow Fe_3O_4 + 6SO_2 \tag{1}$$

$$2Fe_3O_4 + 1/2O_2 \rightarrow + 3Fe_2O_3 \tag{2}$$
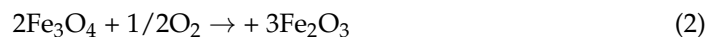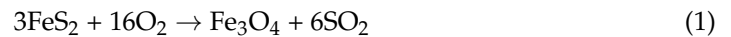
Furthermore, the observation of single grains of hematite with porous and/or onion-shape morphology and outer outlines resembling pseudomorphs of former pyrite crystals, as observed in Figure 7d,e. These textures could be explained by the direct oxidation of precursor pyrite without intermediaries as follows:

$$FeS_2 + O_2 \rightarrow Fe_2O_3 + SO_2 \tag{3}$$

Experimental data indicate that this reaction [3] may proceed within a wide range of temperatures (500–700 °C) but in atmospheres very enriched in oxygen (>5%). Nevertheless, direct transformation of pyrite → magnetite is also possible, but at higher temperatures and lower oxygen conditions [51–55], thus explaining some single porous-like Al-free magnetite grains documented here.

It is worth noting that reflected light microscopy and FESEM characterization reveal submicroscopic particles of native Au and electrum (Au-Ag) in the "morrongos". Most of these particles are associated with highly porous hematite, while some of them are found as isolated grains (Figure 7k,l). Previous works [42,55–61] have recognized Au particles hosted in pyrite as both "visible" particles and "refractory"—i.e., bounded into the pyrite structure or as nanoparticles "invisible" to conventional optical microscopy. Indeed, some of the Au grains now observed as both isolated crystals or associated with the oxides could correspond to those precursor visible Au particles that would have survived the roasting processes. Complementarily, these could be byproducts of pyrite firing. Ref. [52] have recently demonstrated in their experiments that during pyrite roasting, Au originally found to be "refractory" may be released to form discrete particles. These authors stressed that compared to the original pyrite used in their experiments, the surface area and pore volume of the roasted products, especially the meso- and micro-porosity, increased by one order of magnitude when roasting was carried out at 500–600 °C. But the surface area and porosity significantly decreased when the temperature increased up to 700 °C, meaning that particle sintering occurred during roasting. Natural observations and heating experiments of pyrite-type matrices suggest that such sintering of precious metal particles may be the result of both solid-state diffusion and Au-bearing nanomelt migration and accumulation when high-porosity channels are produced during desulfurization-oxidation of sulfides experiencing thermal input [62–65]. In the case of Au, migration and coarsening aided by nanomelt formation should be favored by the lower melting point of metal nanoparticles than their bulk counterparts (e.g., Au particles of <4 nm melt at 370 °C instead of 1064 °C of the bulk; Ref. [63]). A similar interpretation can be assumed to explain the minute bleb-like particles of unidentified compounds of Pb ± Bi ± Cu encased in hematite pseudomorph we observed in the sample TH-3 from Tharsis (Figure 7f). Available empirical and experimental works [66–68] support the existence of melts with a variable proportion of Pb ± Bi ± Cu within the quaternary Bi-Pb-Cu-S system at temperatures departing from 271 °C upwards.

On the other hand, many of the oxide-silicate pellets display rims of Fe-rich sulfates and/or jarosite with varying contents of Pb (e.g., Figure 6c,l). In this type of pyrite waste, these rims were interpreted as the combination of roasting and weathering [33]. The

experimental results by [50,52] indicate that direct oxidation of pyrite takes place with a shrinking unreacted core likely controlled by the chemical reaction of the inward diffusion of oxide due to the pore-blocking effect of the formation of ferric/ferrous sulfate. These Fe-sulfates are able to inherit significant amounts of trace elements initially present in the pyrite lattice or their mineral inclusions (e.g., Pb). Subsequent exposition to atmospheric conditions may cause hydroxylation and hydration during weathering, giving rise to partial transformation into minerals of the jarosite group having variable amounts of Pb. It is worth noting that this mechanism of pyrite roasting and its resulting products have previously been described by [52].

Other sulfates like anglesite ($PbSO_4$), barite ($BaSO_4$), and minium can be ascribed to this late-stage weathering-related oxidation-hydrated mechanism of pre-existing sulfides. Upon exposure to the air and water, galena may undergo aqueous and atmospheric oxidation and then be transformed into secondary sulfates, and/or arsenates, and/or oxides, as those observed in Figure 7i,j.

Finally, quartz is also observed, indicating that it is the most stable phase during combustion, although it shows reaction edges, which suggests that it is partially destabilized due to the high temperatures (Figure 7e), but still resistant to low-temperature surficial alteration.

5.2. Mineralogical Sitting of Economic Metals in the Roasted Pyritic Waste: Economic Potential

The bulk-rock data show that Fe is the major constituent of the roasted pyrite waste analyzed here, with concentrations varying from 37 to 50% (Figure 4a and Table S1). The mineralogical expression of this Fe enrichment is the abundance of Fe oxides and sulfates (Figures 6, 7a–h, 8 and 9). However, other major elements detected in the samples, such as Al (~4%) and Ti (1%), have their mineralogical expression in the relatively high abundance of Al and Ti in oxides like hercynite (up to 52 and 0.3 wt.%, respectively) and silicate glass (up to 32 and 2 wt.%, respectively) as detected by EPMA (Figures 10–12 and Table S2). As noted above, the two mixed samples from Sotiel (S-2) and Tinto-Santa Rosa (TSR-2) show significantly lower Fe values (13%), which are correlated with higher S (up to 10%) and Al (up to 4.34%) (Figure 4a and Table S1). The higher S in these samples is consistent with abundant pyrite (hosting inclusions of tetrahedrite; e.g., Figure 7i) and galena grains found as isolated broken fragments with euhedral morphology (Figure 7h). These latter features suggest incomplete roasting, or more likely, the above-argued nature of some of the collected samples consisting of mixing of the "morrongos" with other types of mining wastes made up of primary ores.

As noted above, the main metals of economic interest are Pb, As, Cu, and, to a lesser extent, Zn. These are detected in averages of >8500, ~4000, ~1235 and ~785 ppm, respectively (Tables S2 and S3). The EPMA analysis shows that Pb is mainly concentrated in the newly-formed anglesite (up to ~75 wt.%) and plumbojarosite (up to ~20 wt.%), as well as in galena relicts (ideally ~86 wt.%) and pyrite (up to ~0.3 wt.%) (Table S2). Arsenic is a fundamental component of the secondary arsenate beudantite (~15 wt.% As_2O_5) and the sulfates plumbojarosite (up to 2.5 wt.% As_2O_5) and anglesite (up to 0.6 wt.% As_2O_5). It is also a main constituent of the accessory inclusions of tetrahedrite-tennantite within relictic pyrite (with up to 0.6 wt.% As) in the samples (Table S2). Cu and Zn are essentially retained in tetrahedrite. In situ LA-ICP-MS also reveals noticeable amounts of Pb (~1800 on average), As (~1200 ppm on average), Cu (~800 ppm), and Zn (1600 ppm) in the Fe-oxides (magnetite and hematite) also resulting from the oxidation of pyrite (Table S3), whereas they are extremely low in the silicate glass and coexisting relictic quartz (As ~90 ppm, Zn ~85 ppm, Pb ~15 ppm, and Cu ~5 ppm; Table S3).

Other metals of economic importance include Sb, Ba, Bi, Mn, and P, which are present in the studied pyrite wastes in concentrations below 300 ppm. These are found as trace elements in all the reported minerals, as they are detected by both EPMA and LA-ICP-MS (Supplementary Tables S2 and S3).

On the other hand, the relatively high bulk-rock concentration of Ag (up to 100 ppm) can be related to the preferential partition of this element into sulfates and sulfide relicts (i.e., jarosite, galena, and tetrahedrite) and, to a lesser extent, oxides (mainly hematite; Figure 11b). In contrast, high bulk-rock contents of Au (up to 5 ppm) are associated with grains of native gold, often hosted in hematite (Figure 7k,l).

Summarizing the observations above, the analyzed "morrongos" have potential for Fe as well as other metals like Pb, Cu, Zn, Ag, and Au, whose abundances (up to 10,000, 4446, 1908, 100, and 5 ppm, respectively) are similar or even higher than the metals mean grades in most current active mines in the area. For example, Cerro Colorado-Riotinto has a grade of 0.03% Pb, 0.3% Cu, and 0.1% Zn, and Masa Valverde has a grade of 0.6% Pb, 0.6% Cu, 1.3% Zn, 29 g/t Ag, and 0.6 g/t Au [69]. Noteworthy, the analyzed "morrongos" from the IPB yield a rather homogenous residue, highlighting that the pyrite roasting process produced more consistent residues if compared with other economically interesting mine wastes. Tailings, for example, although also economically interesting, often show substantial spatial geochemical changes, grain-size gravity-driven segregations, as well as some enriched or depleted pseudo-horizontal alteration fronts [70–73]. Moreover, the mineralogical and textural features of the "morrongos" make them a material suitable for metal recovery by means of a wide range of possible mineral processing methods, including flotation, gravity separation, electrostatic separation, and/or magnetic processes [74–76]. Owing to the low abundance of refractory phases, such as sulfides, together with the high abundance of leachable minerals, including oxides, sulfates, and native metals, we suggest that the most promising metallurgical process could be hydrometallurgical metal extraction [77,78]. Metal recovery from roasted pyrite by means of environmentally friendly hydrometallurgical processes is currently being tested (e.g., Ref. [22] reported up to 84.6% Cu and 68.7% Co recovery by phosphoric acid leaching, and [79] reported up to 90% Au and 41.1% Ag recovery by electrochlorination).

6. Conclusions

This work is the first-ever study attempting to evaluate the potentiality for high-tech metals of a specific type of environmentally risky mining waste produced in the Iberian Pyrite Belt during the 19–20th centuries. Locally known as "morrongos", the residue was the result of pyritic ore metallurgical processing by open-air roasting at relatively high temperatures (>500 °C), as illustrated by the nano-to-micron scale mineralogical study.

Overall, "morrongos" from the IPB show a homogeneous geochemical and mineralogical composition. In addition to the high Fe concentration, the economically interesting elements are Pb, Cu, Zn, Ag, and Au.

The correlation between bulk rock geochemistry, mineralogy, and mineral chemistry data is very high. Major elements (e.g., Fe, S, Al, K, Ti, Mg, Na, and Ca) correlate with hematite, magnetite, hercynite, glass, and silicates. Certain metals and metalloids of economic interest, such as Pb, Cu, Zn, Ag, and Au, are fundamentally associated with oxides, arsenates, sulfates, native metals, and, to a lesser extent, with sulfide remains.

Therefore, "morrongos" from the IPB have the potential to become an asset, thus contributing our new data to a more circular economy for recycling and reprocessing waste materials.

Author Contributions: Conceptualization, L.Y. and J.M.G.-J.; fieldwork, L.Y., J.M.G.-J., F.A.J.-C. and D.C.-M.; methodology, L.Y., J.M.G.-J., F.A.J.-C. and D.C.-M.; formal analysis, J.M.G.-J., L.Y., I.M.S. and I.G.-P.; investigation, all the authors; resources, F.A.J.-C., D.C.-M., L.Y. and J.M.G.-J.; writing—original draft preparation, L.Y. and J.M.G.-J.; writing—review and editing, all the authors; project administration, L.Y.; funding acquisition, L.Y. and J.M.G.-J. All authors have read and agreed to the published version of the manuscript.

Institutional Review Board Statement: Not applicable.

Informed Consent Statement: Not applicable.

Data Availability Statement: Not applicable.

Conflicts of Interest: The authors declare no conflict of interest.

References

1. Watari, T.; Nansai, K.; Nakajima, K. Review of critical metal dynamics to 2050 for 48 elements. *Resour. Conserv. Recycl.* **2020**, *155*, 104669. [CrossRef]

2. Jowitt, S.M.; Mudd, G.M.; Thompson, J.F.H. Future availability of non-renewable metal resources and the influence of environmental, social, and governance conflicts on metal production. *Commun. Earth Environ.* **2020**, *1*, 13. [CrossRef]

3. European Commission. Study on the Critical Raw Materials for the EU 2023-Final Report. Available online: https://single-market-economy.ec.europa.eu/publications/study-critical-raw-materials-eu-2023-final-report_en (accessed on 2 August 2023).

4. Mudd, G.M.; Jowitt, S.M. Growing global copper resources, reserves and production: Discovery is not the only control on supply. *Econ. Geol.* **2018**, *113*, 1235–1267. [CrossRef]

5. Mudd, G.M.; Jowitt, S.M.; Werner, T.T. Global platinum group element resources, reserves and mining—A critical assessment. *Sci. Total Environ.* **2018**, *622*, 614–625. [CrossRef]

6. Horn, S.; Gunn, A.G.; Petavratzi, E.; Shaw, R.A.; Eilu, P.; Törmänen, T.; Bjerkgård, J.; Sandstad, E.; Jonsson, S.; Kountourelis, F.; et al. Cobalt resources in Europe and the potential for new discoveries. *Ore Geol. Rev.* **2021**, *130*, 103915. [CrossRef]

7. Wang, Z.Y.; Fan, H.R.; Zhou, L.; Yang, K.F.; She, H.D. Carbonatite-Related REE Deposits: An Overview. *Minerals* **2020**, *10*, 965. [CrossRef]

8. Linnen, R.; Lichtervelde, M.V.; Černý, P. Granitic Pegmatites as Sources of Strategic Metals. *Elements* **2012**, *8*, 275–280. [CrossRef]

9. Blengini, G.A.; Mathieux, F.; Mancini, L.; Nyberg, M.; Viegas, H.M.; Salminen, J.; Garbarino, E.; Orveillon, G.; Saveyn, H.; Mateos Aquilino, V.; et al. *Recovery of Critical and Other Raw Materials from Mining Waste and Landfills: State of Play on Existing Practices*; EUR 29744 EN; Publications Office of the European Union: Luxembourg, 2019; ISBN 978-92-76-03391-2. [CrossRef]

10. Walton, A.; Anderson, P. Securing Technology-Critical Metals for Britain Ensuring the United Kingdom's Supply of Strategic Elements & Critical Materials for a Clean Future. © University of Birmingham, Birmingham Centre for Strategic Elements & EPSRC Critical Materials & Critical Elements and Materials (CrEAM) Network 2021. Available online: https://www.birmingham.ac.uk/research/energy/research/centre-strategic-elements-critical-materials/securing-technology-critical-metals-for-britain.aspx (accessed on 2 August 2023).

11. Available online: https://www.nsw.gov.au/criticalminerals (accessed on 2 August 2023).

12. Hund, K.L.; Arrobas, D.L.; Fabregas Masllovet, T.P.; Laing, T.J.; Drexhage, J.R. *Climate-Smart Mining Facility in Minerals for Climate Action: The Mineral Intensity of the Clean Energy Transition*; International Bank for Reconstruction and Development: Washington, DC, USA, 2020.

13. European Commission. Report on Critical Raw Materials in the Circular Economy. 2018. Available online: https://weee4future.eitrawmaterials.eu/wp-content/uploads/2020/09/09_report-of-CRM-and-CE.pdf (accessed on 2 August 2023).

14. Gallardo, F.; German, L.; Caro-Moreno, D.; Cantizano, F.A. Successful illegal dumpsite remediation: A landfill mining demonstration project at Andalusia (Spain). *Int. J. Environ. Eng.* **2023**. [CrossRef]

15. Graedel, T.E.; Allwood, J.; Birat, J.P.; Reck, B.K.; Sibley, S.F.; Sonnemann, G.; Buchert, M.; Hagelüken, C. *UNEP. Recycling Rates of Metals—A Status Report, A Report of the Working Group on the Global Metal Flows to the International Resource Panel*; 2011.

16. Forti, V.; Baldé, C.P.; Kuehr, R.; Bel, G. *The Global E-Waste Monitor*; United Nations University, International Telecommunication Union International Solid Waste Association: Bonn, Germany; Geneva, Switzerland; Rotterdam, The Netherlands, 2020.

17. Hunt, J.; Lottemoser, B.G.; Parbhakar-Fox, A.; Van Veen, E.; Goermann, K. Precious metals in gossanous waste rocks from the Iberian Pyrite Belt. *Miner. Eng.* **2016**, *87*, 45–53. [CrossRef]

18. Falagán, C.; Grail, B.; Johnson, D. New approaches for extracting and recovering metals from mine tailings. *Mine. Eng.* **2017**, *106*, 71–78. [CrossRef]

19. Wieczorek, M.; Lottermoser, B.G.; Kiefer, S.; Sindern, S.; Gronen, L.; Hensler, A.S. Indium distribution in metalliferous mine wastes of the Iberian Pyrite Belt, Spain–Portugal. *Environ. Earth Sci.* **2019**, *78*, 253. [CrossRef]

20. Gómez-Arias, L.; Yesares, L.; Caraballo, M.; Maleke, D.; Vermeulen, J.M.; Van Heerden, E.N.; Castillo, J. Environmental and geochemical characterization of alkaline mine wastes from Phalaborwa (Palabora) Complex South Africa. *J. Geochemical Explor.* **2021**, *224*, 106757. [CrossRef]

21. Dold, B. Sourcing of critical elements and industrial minerals from mine waste—The final evolutionary step back to sustainability of humankind? *J. Geochem. Explor.* **2020**, *19*, 106638. [CrossRef]

22. Jiang, T.; Tu, Y.; Su, Z.; Lu, M.; Liu, S.; Liu, J.; Gu, F.; Zhang, Y. A novel value-added utilization process for pyrite cinder: Selective recovery of Cu/Co and synthesis of iron phosphate. *Hydrometallurgy* **2020**, *193*, 105314. [CrossRef]

23. Bendz, D.; Tiberg, C.; Kleja, D.B. Mineralogical characterization and speciation of sulfur, zinc and lead in pyrite cinder from Bergvik, Sweden. *Appl. Geochem.* **2021**, *131*, 105010. [CrossRef]

24. Jamieson, H.; Walker, S.R.; Parsons, M. Mineralogical characterization of mine waste. *Appl. Geochem.* **2015**, *57*, 85–105. [CrossRef]

25. Leistel, J.; Marcoux, E.; Thiéblemon, D.; Quesada, C.; Sánchez, A.; Almodóvar, G.R.; Pascual, E.; Sáez, R. The volcanic-hosted massive sulphide deposits of the Iberian Pyrite Belt Review and preface to the Thematic Issue. *Miner. Depos.* **1998**, *33*, 2–30. [CrossRef]

26. Nocete, F.; Álex, E.; Nieto, J.M.; Sáez, R.; Bayona, M.R. An archaeological approach to regional environmental pollution in the South-Western Iberian Peninsula related to Third Millennium BC mining and metallurgy. *J. Archaeol. Sci.* **2005**, *32*, 1566–1576. [CrossRef]

27. Romero, A.; Gonzalez, I.; Martin, J.M.; Vazquez, M.A.; Ortiz, P. Risk assessment of particle dispersion and trace element contamination from mine-waste dumps. *Environ. Geochem. Health* **2015**, *37*, 273–286. [CrossRef]

28. Sánchez-España, J.; López-Pamo, E.; Pastor, E.S.; Ercilla, M.D. The Acidic Mine Pit Lakes of the Iberian Pyrite Belt: An Approach to Their Physical Limnology and Hydrogeochemistry. *Appl. Geochem.* **2008**, *23*, 1260–1287. [CrossRef]

29. Álvarez-Valero, A.; Sáez, R.; Pérez-López, R.; Delgado, J.; Nieto, J.M. Evaluation of heavy metal bio-availability from Almagrera pyrite-rich tailings dam (Iberian Pyrite Belt, SW Spain) based on a sequential extraction procedure. *J. Geochem. Explor.* **2009**, *102*, 87–94. [CrossRef]

30. Arranz-González, J.C.; Cala-Rivero, V.; Iribarren-Campaña, I. Geochemistry and mineralogy of surface pyritic tailings impoundments at two mining sites of the Iberian Pyrite Belt (SW Spain). *Environ. Earth. Sci.* **2011**, *65*, 669–680. [CrossRef]

31. López-Arce, P.; Garrido, F.; Garcia-Guinea, J.; Voegelin, A.; Göttlicher, J.; Nieto, J.M. Historical roasting of thallium- and arsenic-bearing pyrite: Current Tl pollution in the Riotinto mine area. *Sci. Total Environ.* **2019**, *648*, 1263–1274. [CrossRef] [PubMed]

32. Pinedo Vara, I. *Piritas de Huelva. Su Historia, Minería y Aprovechamiento*; Summa: Madrid, Spain, 1963; p. 1003.

33. Lopez-Arce, P.; Garcia-Guinea, J.; Garrido, F. Chemistry and phase evolution during roasting of toxic thallium-bearing pyrite. *Chemosphere* **2017**, *181*, 447–460. [CrossRef]

34. Cánovas, C.R.; Quispe, D.; Macías, F.; Callejón-Leblic, B.; Arias-Borrego, A.; García-Barrera, T.; Nieto, J.M. Potential release and bioaccessibility of metal/loids from mine wastes deposited in historical abandoned sulfide mines. *Environ. Pollut.* **2023**, *316*, 120629. [CrossRef]

35. Sáez, R.; Pascual, E.; Toscano, M.; Almodóvar, G.R. The Iberian type of volcano-sedimentary massive sulphide deposits. *Miner. Depos.* **1999**, *34*, 549–570. [CrossRef]

36. Almodóvar, G.R.; Yesares, L.; Sáez, R.; Toscano, M.; González, F.; Pons, J.M. Massive sulfide ores in the Iberian Pyrite Belt: Mineralogical and textural evolution. *Minerals* **2019**, *9*, 653. [CrossRef]

37. Yesares, L.; Piña, R.; González-Jiménez, J.M.; Sáez, R.; Ruíz de Almodóvar, G.; Fanlo, F.; Pons, J.M.; Vega, R. Distribution of critical metals in evolving pyrite from massive sul de ores of the Iberian Pyrite Belt. *Ore Geol. Rev.* **2023**, *153*, 105275. [CrossRef]

38. Mercier-Langevin, P.; Hannington, M.D.; Dubé, B.; Bécu, V. The gold content of volcanogenic massive sulfide deposits. *Miner. Depos.* **2011**, *46*, 509–539. [CrossRef]

39. Yesares, L. Mineralizaciones de oro en la Faja Pirítica Ibérica. In *La geología como soporte económico, histórico y social de la región*; Moreno, C., Suárez, J., Eds.; Actas de la II Jornada de Arqueología, Historia y Minería de la Faja Pirítica Ibérica; 2019; ISBN 978-84-09-067 77-0.

40. Conde, C.; Tornos, F.; Danyushevsky, L.V.; Large, R. Laser ablation-ICPMS analysis of trace elements in pyrite from the Tharsis massive sulphide deposit, Iberian Pyrite Belt (Spain). *J. Iber. Geol.* **2020**, *47*, 429–440. [CrossRef]

41. Yesares, L.; Sáez, R.; Nieto, J.M.; Almodóvar, G.R.; Gómez, C.; Escobar, J.M. The Las Cruces deposit, Iberian Pyrite Belt, Spain. *Ore Geol. Rev.* **2015**, *66*, 25–46. [CrossRef]

42. González-Jiménez, J.M.; Yesares, L.; Piña, R.; Sáez, R.; Almodóvar, G.R.; Nieto, F.; Tenorio, S. Polymetallic nanoparticles in pyrite from VMS deposits of the Iberian Pyrite Belt. *Ore Geol. Rev.* **2022**, *145*, 104875. [CrossRef]

43. Tornos, F. Environment of formation and styles of volcanogenic massive sulfides: The Iberian Pyrite Belt. *Ore Geol. Rev.* **2006**, *28*, 259–307. [CrossRef]

44. Saéz, R. La Faja Pirítica Ibérica. Una Perspectiva Geológica, Arqueológica y Ambiental. Unpublished Ph.D. Thesis, University of Huelva, Huelva, Spain, 2010.

45. Consejería de Cultura (Junta de Andalucía). Expedientes de Minas (1917–1995). Fondo Documental. Delegación Provincial del Ministerio de Industria en Huelva 2001. Available online: https://www.juntadeandalucia.es/cultura/archivos_html/sites/default/contenidos/archivos/ahphuelva/documentos/00029.pdf (accessed on 2 August 2023).

46. IGME. Inventario Nacional de Balsas y Escombreras Mineras. Instituto Geológico y Minero de España (IGME) 1989. Available online: https://info.igme.es/catalogo/resource.aspx?portal=1&catalog=3&ctt=1&lang=spa&dlang=eng&llt=dropdown&master=infoigme&shdt=false&shfo=false&resource=8305 (accessed on 2 August 2023).

47. Cánovas, C.R.; Macías, F.; González, C.; Pérez-López, R.; Nieto, J.M. Metal/loid release from cyanidation wastes in response to rainfalls. *Procedia Earth Planet. Sci.* **2017**, *17*, 436–439. [CrossRef]

48. Moreno-González, R.; Olías, M.; Macías, F.; Cánovas, C.R.; Fernández de Villarán, R. Hydrological characterization and prediction of flood levels of acidic pit lakes in the Tharsis mines, Iberian Pyrite Belt. *J. Hydrol.* **2018**, *566*, 807–817. [CrossRef]

49. *REDIAM Ortofotografía Digital Rigurosa de Andalucía. Consejería de Sostenibilidad, Medio Ambiente y Economía Azul*; Junta de Andalucía España: Sevilla, Spain, 2020.

50. Hu, G.; Dam-Jhansen, K.; Wedel, S.; Hansen, J.P. Decomposition and oxidation of pyrite. *Prog. Energy Combust. Sci.* **2006**, *32*, 295–314. [CrossRef]

51. Laita, E.; Bauluz, B.; Yuste, A. High-Temperature Mineral Phases Generated in Natural Clinkers by Spontaneous Combustion of Coal. *Minerals* **2019**, *9*, 213. [CrossRef]

52. Zhang, Y.P.; Yang, K.; Fang, Y.; Robledo-Cabrera, A.; Peng, C.S.; Lopez-Valdivieso, A. Roasting temperature effect on the recovery of refractory gold and silver in pyrite concentrates. *J. Min. Metall. Sect. B-Metall.* **2021**, *57*, 235–243. [CrossRef]

53. Menegazzo, G.; Carbonin, S.; Della Giusta, A. Cation and vacancy distribution in an artificially oxidized natural spinel. *Miner. Mag.* **1997**, *6*, 411–421. [CrossRef]

54. Jastrzebska, I.; Szczerba, J.; Blachowski, A.; Stoch, P. Structure and microstructure evolution of hercynite spinel (Fe2+Al2O4) after annealing treatment. *Eur. J. Mineral.* **2017**, *29*, 63–72. [CrossRef]

55. Marcoux, E.; Moëlo, Y.; Leistel, J.M. Bismuth and cobalt minerals: Indicators of stringer zones to massive sulfide deposits. Iberian Pyrite Belt. *Miner. Depos.* **1996**, *31*, 1–26. [CrossRef]

56. Becattini, V.; Motmans, T.; Zappone, A.; Madonna, M.; Haselbacher, A.; Steinfeld, A. Experimental investigation of the thermal and mechanical stability of rocks for high-temperature thermal-energy storage. *Appl. Energy* **2017**, *203*, 373–389. [CrossRef]

57. Nishihara, K.; Kondo, Y. Studies of the Oxidation of Pyrite I. *Mem. Fac. Eng. Kyoto Univ.* **1959**, *20*, 285.

58. Schorr, J.R.; Everhart, J.O. Thermal Behavior of Pyrite and Its Relation to Carbon and Sulfur Oxidation in Clays. In Proceedings of the Sixty-Sixth Annual Meeting, Atlantic City, NJ, USA, 6 May 1974; The American Ceramic Society: Chicago, IL, USA, 1969.

59. Huffman, G.P.; Huggins, F.E.; Levasseur, A.A.; Chow, O.; Srinivasachar, S.; Mehta, A.K. Investigation of the transformations of pyrite in a drop-tube furnace. *Fuel* **1989**, *68*, 485–490. [CrossRef]

60. Bhargava, S.K.; Garg, A.; Subasinghe, N. In situ high-temperature phase transformation studies on pyrite. *Fuel* **2009**, *88*, 988–993. [CrossRef]

61. Zhang, Y.; Li, Q.; Liu, X.; Xu, B.; Yang, Y.; Jiang, T. A Thermodynamic Analysis on the Roasting of Pyrite. *Mineral* **2019**, *9*, 220. [CrossRef]

62. Reich, M.; Kesler, S.E.; Utsunomiya, S.; Palenik, C.S.; Chryssoulis, S.L.; Ewing, R.C. Solubility of gold in arsenian pyrite. *Geochim. Cosmochim. Acta* **2005**, *69*, 2781–2796. [CrossRef]

63. Reich, M.; Utsunomiya, S.; Kesler, S.E.; Wang, L.M.; Ewing, R.C.; Becker, U. Thermal behaviour of metal nanoparticles in geologic materials. *Geology* **2006**, *34*, 1033–1036. [CrossRef]

64. González-Jiménez, J.M.; Reich, M.; Camprubí, A.; Gervilla, F.; Griffin, W.L.; Colás, V.; O'Reilly, S.Y.; Proenza, J.A.; Pearson, N.J.; Centeno-García, E. Thermal metamorphism of mantle chromites and the stability of noble-metal nanoparticles. *Contrib. Miner. Petrol.* **2015**, *170*, 15. [CrossRef]

65. Domínguez-Carretero, D.; González-Jiménez, J.M.; Proenza, J.A. A track record of Au–Ag nanomelt generation during fluid-mineral interactions. *Sci. Rep.* **2023**, *13*, 7895. [CrossRef]

66. Craig, J.R. Phase relations and mineral assemblages in the Ag–Bi–Pb–S system. *Miner. Depos.* **1967**, *1*, 278–306. [CrossRef]

67. Ciobanu, C.L.; Cook, N.J.; Pring, A. Bismuth tellurides as gold scavengers. In *Mineral Deposit Research: Meeting the Global Challenge*; Mao, J.W., Bierlein, F.P., Eds.; Springer: Berlin/Heidelberg, Germany, 2005; pp. 1383–1386.

68. Ciobanu, C.; Cook, N.; Damian, F. Gold scavenged by bismuth melts: An example from Alpine shear-remobilizates in the Highiş Massif, Romania. *Mineral. Petrol.* **2006**, *87*, 351–384. [CrossRef]

69. Noble, A.C. Technical Report On the Riotinto Copper Project 2022. Available online: www.atalayamining.com (accessed on 2 August 2023).

70. Dold, B.; Fontboté, L. A mineralogical and geochemical study of element mobility in sulfide mine tailings of Fe oxide Cu–Au deposits from the Punta del Cobre belt, northern Chile. *Chem. Geol.* **2002**, *189*, 135–163. [CrossRef]

71. Heikkinen, P.M.; Räsänen, M.L. Mineralogical and geochemical alteration of Hitura sulphide mine tailings with emphasis on nickel mobility and retention. *J. Geochem. Explor.* **2008**, *97*, 1–20. [CrossRef]

72. Wang, L.; Li, Y.; Wang, H.; Cui, X.; Wang, X.; Lu, A.; Wang, X.; Wang, C.; Gan, D. Weathering behavior and metal mobility of tailings under an extremely arid climate at Jinchuan Cu-Ni sufide deposit, Western China. *J. Geochem. Explor.* **2017**, *173*, 1–12. [CrossRef]

73. Gómez-Arias, A.; Yesares, L.; Díaz, J.; Caraballo, M.A.; Maleke, M.; Sáez, R.; Van Heerden, E.; Nieto, J.M.V.; Castillo, J. Mine waste from carbonatite deposits as potential rare earth resource: Insight into the Phalaborwa (Palabora) Complex. *J. Geochem. Explor.* **2022**, *232*, 106884. [CrossRef]

74. Chen, D.; Gou, H.; Lv, Y.; Li, P.; Xu, J. Preparation and recovery of iron carbide from pyrite cinder using carburization-magnetic separation technology. *J. Min. Metall. Sect. B Metall.* **2018**, *54*, 271. [CrossRef]

75. Zhang, X.; Chen, G.; Cai, X.; Fu, J.; Liu, M.; Zhang, P.; Yu, H. Leaching behavior of copper and iron extracted from pyrite cinder of reduction roasting. *J. Hazard. Mater.* **2021**, *420*, 126561. [CrossRef]

76. Liu, R.; Jing, N.; Song, Y.; Zhaia, Q.; Mao, Z.; Zhou, Y.; Sun, W. Recovery of valuable elements from pyrite pyrolysis slag using magnetic separation-flotation technique. *Sep. Purif. Technol.* **2022**, *299*, 121772. [CrossRef]
77. Wanga, Y.; Xiaoa, L.; Liuc, H.; Qiana, P.; Yea, S.; Chena, Y. Acid leaching pretreatment on two-stage roasting pyrite cinder for gold T extraction and co-precipitation of arsenic with iron. *Hydrometallurgy* **2018**, *179*, 192–197. [CrossRef]
78. Kenzhaliyev, B.; Surkova, T.; Yessimova, D.; Baltabekova, Z.; Abikak, Y.; Abdikerim, B.; Dosymbayeva, Z. Extraction of Noble Metals from Pyrite Cinders. *Chem. Eng.* **2023**, *7*, 14. [CrossRef]
79. Kenzhaliyev, B.; Surkova, T.; Yessimova, D.; Abikak, Y.; Mukhanova, A.; Fischer, D. Extraction of Noble Metals from Pyrite Cinders. *Inorganics* **2023**, *11*, 171. [CrossRef]
80. Pagé, P.; Barnes, S.-J. The influence of chromite on osmium, iridium, ruthenium and rhodium distribution during early magmatic processes. *Chem. Geol.* **2016**, *420*, 51–68. [CrossRef]